inorganics

MDPI

Article

Anion Capture at the Open Core of a Geometrically Flexible Dicopper(II,II) Macrocycle Complex

Sam H. Brooks, Corey A. Richards, Patrick J. Carroll, Michael R. Gau and Neil C. Tomson *

Department of Chemistry, University of Pennsylvania, 231 South 34th Street, Philadelphia, PA 19104, USA
* Correspondence: tomson@upenn.edu; Tel.: +1-215-898-6208

Abstract: Multicopper active sites for small molecule activation in materials and enzymatic systems rely on controlled but adaptable coordination spheres about copper clusters for enabling challenging chemical transformations. To translate this constrained flexibility into molecular multicopper complexes, developments are needed in both ligand design for clusters and synthetic strategies for modifying the cluster cores. The present study investigates the chemistry of a class of pyridyldiimine-derived macrocycles with geometrically flexible aliphatic linkers of varying lengths ($^{n}PDI_2$, n = 2, 3). A series of dicopper complexes bound by the $^{n}PDI_2$ ligands are described and found to exhibit improved solubility over their parent analogs due to the incorporation of 4-^{t}Bu groups on the pyridyl units and the use of triflate counterions. The ensuing synthetic study investigated methods for introducing various bridging ligands (μ-X; X = F, Cl, Br, N_3, NO_2, $OSiMe_3$, OH, OTf) between the two copper centers within the macrocycle-supported complexes. Traditional anion metathesis routes were unsuccessful, but the abstraction of bridging halides resulted in "open-core" complexes suitable for capturing various anions. The geometric flexibility of the $^{n}PDI_2$ macrocycles was reflected in the various solid-state geometries, Cu–Cu distances, and relative Cu coordination spheres on variation in the identity of the captured anion.

Keywords: copper complexes; cupric; Cu(II); dinuclear; macrocycles; ligand flexibility; bridging hydroxide; bridging nitrite; bridging fluoride

Citation: Brooks, S.H.; Richards, C.A.; Carroll, P.J.; Gau, M.R.; Tomson, N.C. Anion Capture at the Open Core of a Geometrically Flexible Dicopper(II,II) Macrocycle Complex. *Inorganics* **2023**, *11*, 348. https://doi.org/10.3390/inorganics11090348

Academic Editor: Philippe Schollhammer

Received: 1 August 2023
Revised: 19 August 2023
Accepted: 22 August 2023
Published: 24 August 2023

1. Introduction

Controlled internuclear geometries are a defining feature in multicopper active sites for small molecule functionalization. These sites arise in materials, like various Cu-impregnated zeolites that perform selective methane oxidation [1–3], and in a host of enzymes, including those that either selectively oxidize methane (particulate methane monooxygenase), phenols (tyrosinase), and quinones (tyrosinase and catechol oxidase) or transport oxygen (hemocyanin) [4]. It is of interest to develop molecular complexes that mimic the properties of multinuclear active sites, as doing so may yield insight into key structure–function relationships for strong bond activation schemes. However, enzymatic copper–copper distances, for example, range from 2.2–4.9 Å and are known to change upon substrate binding [4]. Modulating both the distance and relative coordination environments between multiple copper centers in molecular systems may influence how small molecules react at a multicopper active site, but ligand design for multinuclear transition metal systems is in its infancy, especially for systems that accommodate structural rearrangements.

Examples of ligands capable of housing multiple copper centers [5] and binding molecules of various sizes have been realized in the areas of anion recognition/sensing [6–8], dioxygen activation [9,10], organic azide reduction [11], aryl group transfer, and alkyne activation [12,13]. From these studies, an important feature of ligand design is the capacity to tune the distance between the copper centers. Drew and Nelson originally targeted this aspect in the 1980s when designing and synthesizing macrocyclic *bis*(pyridyldiimine)

ligands [14–17]. The two pyridyldiimine (PDI) units linked by aliphatic spacers were suitable for binding two copper(II) centers at specific distances (Figure 1) while allowing for flexibility in the coordination environments of the metal centers with respect to one another. For example, the use of a 3,6-dioxaoctylene spacer allowed for the formation of a bridging azide complex, [(^{Oct}PDI$_2$)Cu$_2$(N$_3$)$_3$][ClO$_4$] [15], with a μ-1,3-binding azide that spans the long Cu–Cu distance of 6.02 Å, but a μ-hydroxide complex with the same ligand, [(^{Oct}PDI$_2$)Cu$_2$OH][ClO$_4$]$_3$·H$_2$O [14], makes use of the flexibility of the aliphatic linker as the macrocycle contorts to accommodate a shorter Cu–Cu distance of 3.57 Å.

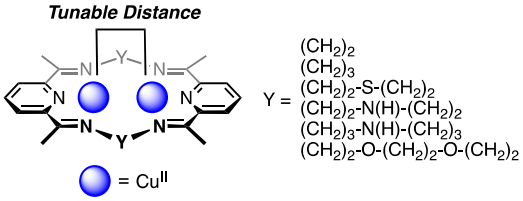

Figure 1. *Bis*(pyridyldiimine) macrocyclic ligands developed by Drew and Nelson.

The *bis*(pyridyldiimine) macrocyclic ligands have provided a useful platform to study multinuclear copper chemistry, but synthetic elaborations and structural information on these systems are limited. Previous work in our lab has shown that the syntheses of dinuclear first-row transition metal *bis*(pyridyldiimine) macrocyclic complexes were aided by the installation of *tert*-butyl groups at the 4-position of the PDI units [18–25]. The *tert*-butyl groups allow for an enhancement in solubility in less polar organic solvents (THF, DCM, and MeCN) compared to the original macrocycles reported by Drew and Nelson. We thus sought to synthesize a new series of Cu$_2$(II,II) *bis*(pyridyldiimine) macrocycles for structural characterization. Herein, new synthetic routes to Cu$_2$(II,II) *bis*(pyridyldiimine) macrocyclic complexes are explored with versatile ligand substitution being achieved.

2. Results and Discussion

2.1. Ring-Size Modulated Structures of [Cu$_2$Cl$_2$]$^{2+}$ Cluster Cores

The synthesis of a Cu$_2$(II,II) *bis*(4-*tert*-butylpyridyldiimine) macrocyclic complex was carried out using the strontium-templated macrocycle [(^{3}PDI$_2$)Sr][OTf]$_2$ (**^{3}[Sr]$^{2+}$**, where 3 refers to the aliphatic chain length connecting the PDI units). The treatment of a yellow methanolic solution of **^{3}[Sr]$^{2+}$** with 2.0 equiv of CuCl$_2$·2H$_2$O afforded the paramagnetic, dark green dinuclear macrocycle-bound complex [(^{3}PDI$_2$)Cu$_2$Cl$_2$][OTf]$_2$ (**^{3}[Cu$_2$Cl$_2$]$^{2+}$**) in good yield (Scheme 1). Crystallographic analysis revealed that the copper(II) centers are related by an inversion center (Figure 2). The metal sites adopt a distorted octahedral geometry, with a PDI subunit and a bridging chloride occupying the equatorial positions and a triflate anion and a bridging chloride occupying the axial positions (selected bond metrics are presented in Table 1). No six-coordinate mononuclear copper(II) chloride PDI complexes have been reported in the literature. However, the Cu–N bond lengths are in good agreement with the related four-coordinate [(^{dipp}PDI)CuCl][PF$_6$] reported by Conan. The equatorial Cu–Cl bond length of 2.18602(11) Å agrees well with Conan's observed Cu–Cl bond length of 2.1450(5) Å. The axial Cu–O (2.710 Å) and Cu–Cl (2.873 Å) distances are elongated, owing to a strong Jahn–Teller distortion at the d^9 Cu(II) ion. Due to this distortion, the Cu$_2$Cl$_2$ diamond core exhibits a very acute Cu-Cl-Cu angle (75.05°). The structure reported here for **^{3}[Cu$_2$Cl$_2$]$^{2+}$** closely resembles that of [(^{3}PDI$_2$)Cu$_2$Cl$_2$(thf)$_2$][BAr$^F{}_4$]$_2$ (Ar^F = 3,5-(CF$_3$)$_2$-C$_6$H$_3$), which was synthesized using a similar scheme but with THF as the solvent and with the addition of NaBAr$^F{}_4$. The difference in axial ligation between the two ^{3}PDI$_2$ structures highlights the weak ionic binding of the axial triflate ions. For this reason and to simplify the descriptions, all triflate ions described in the text will use an ionic formulation, even when they appear bound to a metal center in the solid state.

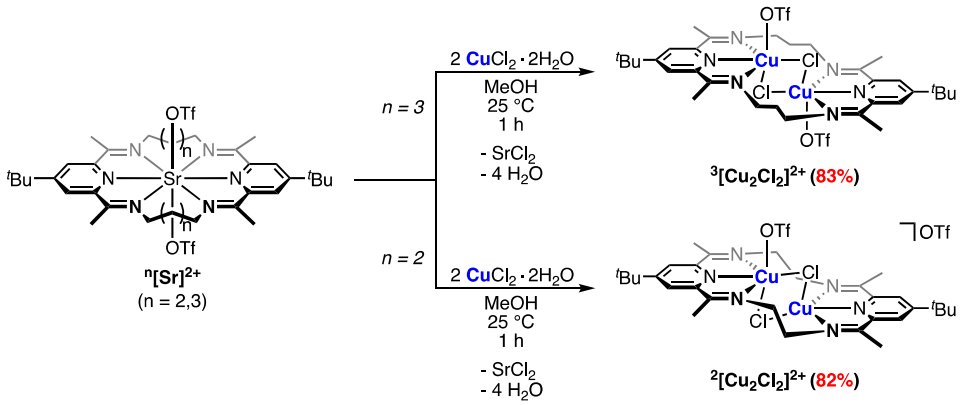

Scheme 1. Synthesis of $^{n}[Cu_2Cl_2]^{2+}$ complexes in MeOH.

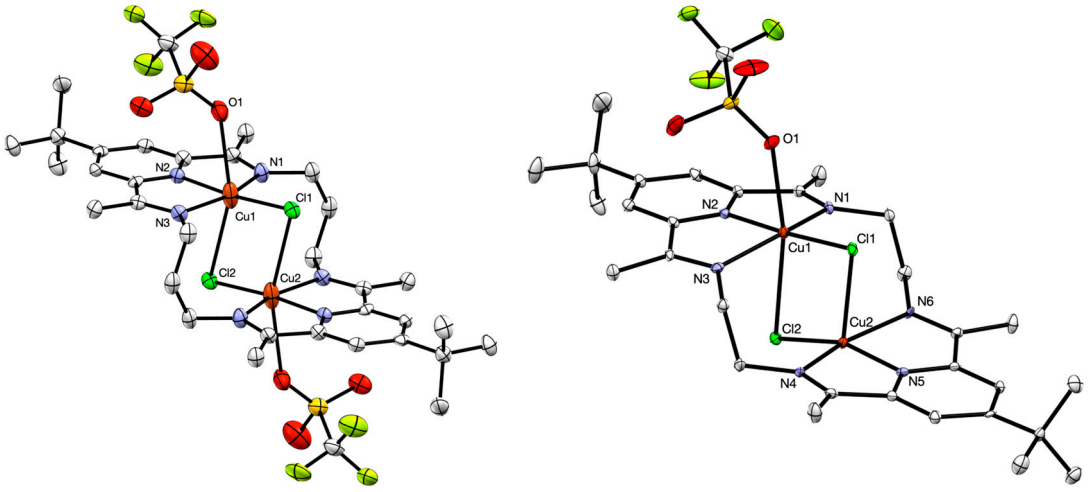

Figure 2. Left: Crystal structure of $^{3}[Cu_2Cl_2]^{2+}$ (thermal ellipsoids set at 50% probability; hydrogen atoms and triflate disorder omitted for clarity). **Right**: Crystal structure of $^{2}[Cu_2Cl_2]^{2+}$ (thermal ellipsoids set at 50% probability; hydrogen atoms, solvent molecules, and outer-sphere anions omitted for clarity; one macrocycle of the asymmetric unit shown). The following atoms shown in this figure are color-coded for convenience: Cu (orange), N (blue), C (light grey), Cl (bright green), F (yellow-green), S (yellow), and O (red).

An additional parameter that can be gleaned from the crystal structure of $^{3}[Cu_2Cl_2]^{2+}$ is the oxidation state of the (redox-active) PDI ligand [26]. Wieghardt and coworkers previously reported the Δ parameter as a means of identifying how much electron density resides in the PDI π* manifold. Our lab recently adapted the Δ parameter in describing the *bis*(4-*tert*-butylpyridyldiimine) macrocyclic ligand oxidation state, which includes the average of each Δ parameter for each PDI subunit [22]. Using this analysis on the crystal structure of $^{3}[Cu_2Cl_2]^{2+}$, the average Δ parameter of 0.187 Å supports the assignment of a neutral physical oxidation state on the $^{3}PDI_2$ ligand. A neutral ligand for copper PDI complexes is not uncommon, as both mononuclear $Cu^{II}(PDI^{0})$ and $Cu^{I}(PDI^{0})$ examples are well established in the literature [26].

The IR spectrum of $^{3}[Cu_2Cl_2]^{2+}$ contained a characteristic imine stretching frequency at 1601 cm^{-1}. UV-vis-NIR spectroscopic analysis revealed an absorption profile representative of *bis*(pyridyldiimine) macrocyclic complexes in an unfolded ligand conformation [21]. Distinct absorption bands at 237 nm (7.71×10^4 M^{-1} cm^{-1}) and 676 nm (242 M^{-1} cm^{-1}) result from a π→π* transition and a d→d transition, respectively.

Table 1. Selected bond metrics of copper(II) chloride PDI complexes.

	^{3}**[Cu$_2$Cl$_2$]$^{2+a}$**	^{2}**[Cu$_2$Cl$_2$]$^{2+b}$**	**[(^{dipp}PDI)CuCl][PF$_6$]**
Cu(1)—N(1)/Å	2.056(4)	2.057	2.070(2)
Cu(1)—N(2)/Å	1.902(3)	1.903	1.922(2)
Cu(1)—N(3)/Å	2.047(3)	2.044	2.062(2)
Cu(1)—Cl(1)/Å	2.1860(11)	2.2056	2.1450(5)
Cu(1)—Cl(2)/Å	2.873(1)	3.021	-
Cu(1)—O(1)/Å	2.710(1)	2.4015	-
Cu(1)—Cu(2)/Å	3.129(1)	2.9922	-
Cu(2)—N(4)/Å	-	2.041	-
Cu(2)—N(5)/Å	-	1.898	-
Cu(2)—N(6)/Å	-	2.042	-
Cu(2)—Cl(1)/Å	-	2.7273	-
Cu(2)—Cl(2)/Å	-	2.2043	-
∠Cu(1)-Cl(1)-Cu(2)/°	75.05(4)	73.83	-
∠Cu(1)-Cl(2)-Cu(2)/°	-	67.80	-
Δ/Å	0.187	0.182	0.178

[a] Macrocycle is symmetric; bond metrics are the same for Cu(2). [b] Average values; two macrocycles are present in the asymmetric unit.

The successful synthesis and characterization of **^{3}[Cu$_2$Cl$_2$]$^{2+}$** prompted further investigation into the effect of macrocycle size in the preparation of Cu$_2$(II,II) macrocyclic complexes. Upon the addition of 2.0 equiv CuCl$_2$·2H$_2$O to the smaller macrocycle **^{2}[Sr]$^{2+}$**, an immediate color change from yellow to dark blue-green was observed. The macrocycle [(^{2}PDI$_2$)Cu$_2$Cl$_2$][OTf]$_2$ (**^{2}[Cu$_2$Cl$_2$]$^{2+}$**) was isolated in good yield (Scheme 1). The solid-state structure of **^{2}[Cu$_2$Cl$_2$]$^{2+}$** depicts a similar ligand conformation to **^{3}[Cu$_2$Cl$_2$]$^{2+}$** (Figure 2). Two chloride ligands reside between the copper centers; however, variations in the Cu$_2$Cl$_2$ core are evident when compared to **^{3}[Cu$_2$Cl$_2$]$^{2+}$**. Unlike the larger macrocycle, each copper center adopts a different coordination geometry. One copper is found in a distorted octahedral geometry, capped by a triflate anion and a bridging chloride (analogous to **^{3}[Cu$_2$Cl$_2$]$^{2+}$**). The second copper adopts a square pyramidal geometry (avg. τ_5 = 0.04) [27], with the second triflate anion residing in the outer coordination sphere. The difference in the coordination geometries about the copper centers is reflected in the distortion of the Cu$_2$Cl$_2$ core, which now appears asymmetric (∠Cu(1)-Cl-Cu(2) = 73.83(4)° and ∠Cu(2)-Cl-Cu(1) = 67.80(4)°). This distortion is further reflected in the asymmetry of the axial Cu–Cl distances, which diverge from the value of 2.873(1) Å for each interaction in **^{3}[Cu$_2$Cl$_2$]$^{2+}$** to values of 2.7273 and 3.021 Å in **^{2}[Cu$_2$Cl$_2$]$^{2+}$**. While these distances are long, they are well within the sum of the van der Waals radii for Cu and Cl (4.20 Å) [28], and previous work from our group on closely related molecules has identified magnetic communication through bridging chloride ligands with Cu–Cl distances up to 3.159(1) Å [21]. Aside from the noted differences in the Cu$_2$Cl$_2$ core, the remaining bond metrics of **^{2}[Cu$_2$Cl$_2$]$^{2+}$** remain comparable to those in **^{3}[Cu$_2$Cl$_2$]$^{2+}$** and [(^{dipp}PDI)CuCl][PF$_6$] (Table 1).

2.2. Chloride Abstraction from ^{3}[Cu$_2$Cl$_2$]$^{2+}$

With **^{3}[Cu$_2$Cl$_2$]$^{2+}$** isolated, anion metathesis was targeted to introduce new ligands at the Cu(II) centers, but little to no reactivity was observed, likely owing to strong bridging-chloride interactions. Chloride abstraction routes were thus employed to enhance the reactivity of the pocket toward anion metathesis. Attempts at chloride abstraction with traditional reagents (KOTf, Ag$_n$X (n = 1,2; X = BF$_4$, SO$_4$, OTf, BAr$^{F}_4$)) were met with either intractable mixtures or no reactivity. Chloride abstraction was achieved with the addition of an excess of TMS-OTf (TMS = trimethylsilyl) to **^{3}[Cu$_2$Cl$_2$]$^{2+}$** in MeCN. The formation of a new macrocyclic product was apparent by a sharp color change from dark green to dark blue. The concentration of the reaction mixture afforded the blue acetonitrile-coordinated macrocycle complex [(^{3}PDI$_2$)Cu$_2$(NCMe)$_2$][OTf]$_4$ (**^{3}[Cu$_2$(NCMe)$_2$]$^{4+}$**) (Scheme 2). Unlike

^{3}**[Cu$_2$Cl$_2$]$^{2+}$**, ^{3}**[Cu$_2$(NCMe)$_2$]$^{4+}$** exhibited low solubility in common organic solvents (THF, DCM, MeCN).

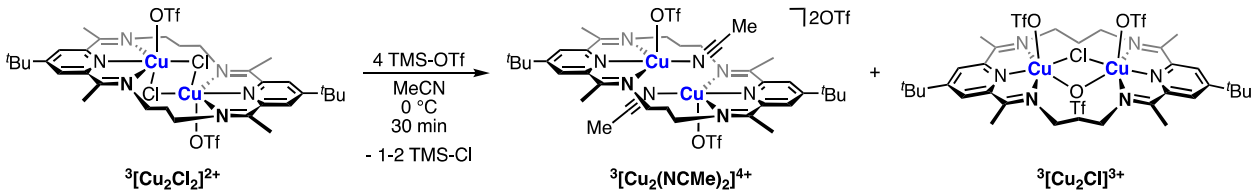

Scheme 2. Abstraction of bridging chlorides from ^{3}**[Cu$_2$Cl$_2$]$^{2+}$** using TMS-OTf in MeCN.

Despite its limited solubility in MeCN, single crystals of ^{3}**[Cu$_2$(NCMe)$_2$]$^{4+}$** were able to be grown from the slow diffusion of Et_2O into a concentrated MeCN solution. The solid-state structure was found to resemble that of ^{3}**[Cu$_2$Cl$_2$]$^{2+}$**, with the two chloride ligands replaced by MeCN ligands (Figure 3). The macrocyclic ligand adopts an unfolded ligand conformation, and the two Cu(II) centers are related by a center of symmetry with a spacing of 3.3479(7) Å. Both Cu(II) centers adopt a distorted square pyramidal geometry (τ_5 = 0.36 for each Cu(II) center) with an evident Jahn–Teller distortion causing a long Cu–O (2.275(2) Å) bond length. The axial Cu-*N*CMe bond lengths (3.160(3) Å) fall outside the sum of the van der Waals radii of copper and nitrogen (2.95 Å). Thus, five-coordinate copper(II) is a better description of the metal centers in this crystal structure. The equatorial Cu-*N*CMe distance of 1.973(3) Å is significantly shorter than the reported distance of 2.271(13) in McKee and coworkers' related Cu_2(II,II) alkoxy PDI macrocycle [29]. However, the MeCN ligand occupies a distorted axial position of a square pyramidal Cu(II) center in McKee's example, rather than the equatorial position as observed in ^{3}**[Cu$_2$(NCMe)$_2$]$^{4+}$**. Gilbertson's distorted square planar copper(I) acetonitrile PDI complex displays a short Cu-*N*CMe distance of 1.907(7) Å, which better agrees with ^{3}**[Cu$_2$(NCMe)$_2$]$^{4+}$** [30].

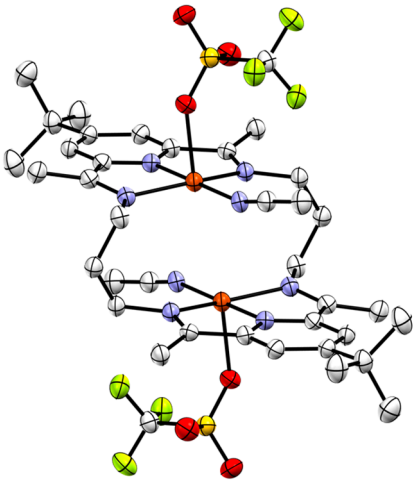

Figure 3. Crystal structure of ^{3}**[Cu$_2$(NCMe)$_2$]$^{4+}$** (thermal ellipsoids set at 50% probability; hydrogen atoms, solvent molecules, and outer-sphere anions omitted for clarity). The following atoms shown in this figure are color-coded for convenience: Cu (orange), N (blue), C (light grey), F (yellow-green), S (yellow), and O (red).

The IR spectrum of a sample of ^{3}**[Cu$_2$(NCMe)$_2$]$^{4+}$** includes three distinct nitrile stretching frequencies in the expected region for acetonitrile (2307 cm^{-1}, 2279 cm^{-1}, 2257 cm^{-1}). Since ^{3}**[Cu$_2$(NCMe)$_2$]$^{4+}$** would have two stretches at most—a low-intensity symmetric stretch and a higher-intensity asymmetric stretch—the IR data suggest the presence of impurities in the isolated material. Although satisfactory elemental analysis data were collected, alternative routes of crystallization were assessed to address the discrepancy in the

IR spectral data. The product was found to be partially soluble in *o*-difluorobenzene. Crystallization from this solvent afforded single crystals that were identified as the monochloride product [(^{3}PDI$_2$)Cu$_2$Cl][OTf]$_3$ (**^{3}[Cu$_2$Cl]$^{3+}$**), indicative of incomplete chloride abstraction and the presence of impurities. Prolonged reaction times in the presence of excess TMS-OTf were not able to improve the purity of **^{3}[Cu$_2$(NCMe)$_2$]$^{4+}$**. Although not the desired product, the crystal structure of **^{3}[Cu$_2$Cl]$^{3+}$** offered insight into how the ligand is able to change in conformation to accommodate one bridging ligand upon the loss of a bridging chloride from **^{3}[Cu$_2$Cl$_2$]$^{2+}$**.

The solid-state structure of **^{3}[Cu$_2$Cl]$^{3+}$** introduces an arched ligand conformation around the dinuclear Cu$_2$Cl core (Figure 4). Both Cu(II) centers adopt distorted octahedral geometries, with three triflate anions (two terminal and one bridging) occupying the positions perpendicular to the planes of the local PDI units. Jahn–Teller distortions are evident by the elongated Cu–O axial bond lengths (avg. 2.5042 Å). A single chloride bridges the two copper(II) centers with a Cu-Cl-Cu angle of 108.50(3)° (an increase of 33° compared to **^{3}[Cu$_2$Cl$_2$]$^{2+}$**), and the Cu–Cl bond distances elongate to 2.2906(7) and 2.2739(7) Å. These longer bond distances are still in the expected range for Cu(II) chloride PDI complexes, agreeing well with related five-coordinate complexes. To accommodate the increases in the Cu-Cl-Cu angle and the Cu–Cl distances upon the loss of a bridging chloride from **^{3}[Cu$_2$Cl$_2$]$^{2+}$**, the macrocycle conformation changes, and the Cu–Cu distance increases from 3.129(1) Å to 3.7045(7) Å.

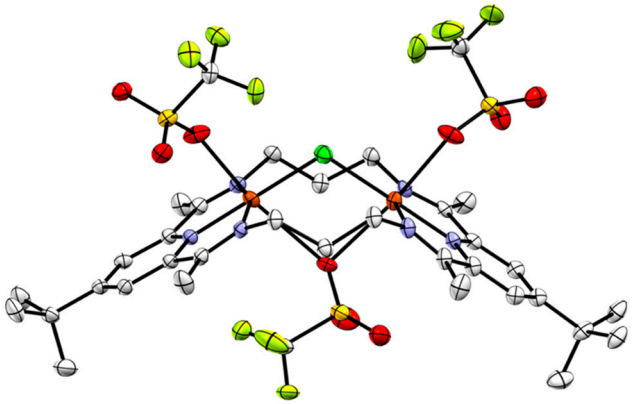

Figure 4. Crystal structure of **^{3}[Cu$_2$Cl]$^{3+}$** (thermal ellipsoids set at 50% probability; hydrogen atoms and triflate disorder omitted for clarity). The following atoms shown in this figure are color-coded for convenience: Cu (orange), N (blue), C (light grey), Cl (bright green), F (yellow-green), S (yellow), and O (red).

2.3. A Synthetic Route to an "Open-Core" Cu$_2$(II,II) Macrocycle

Due to incomplete chloride abstraction from **^{3}[Cu$_2$Cl$_2$]$^{2+}$**, we sought a new approach to the synthesis of an "open-core" macrocycle. Attempts to eliminate the halide from the original synthesis (i.e.,**^{3}[Sr]$^{2+}$** + 2 Cu(OTf)$_2$) failed to produce an observable reaction when run in DCM, and the products of this reaction were not separable from one another when the reaction was run in MeCN. We next proposed that the strong bridging interactions in **^{3}[Cu$_2$Cl$_2$]$^{2+}$** may be limiting the reactivity of this species towards TMS-OTf. To address this concern, we sought to exchange the bridging chloride ligands for a fluoride ligand. Doing so could then leverage the stronger thermodynamic driving force for Si–F over Si–Cl bond formation on treatment with TMS-OTf.

The synthetic changes were carried out in a one-pot fashion (Scheme 3). A mixture of **^{3}[Sr]$^{2+}$** and 2.0 equiv Cu(OTf)$_2$ was stirred in DCM and treated with [NBu$_4$][Ph$_3$SiF$_2$] to produce a new paramagnetic, blue macrocyclic product. The monofluoride product [(^{3}PDI$_2$)Cu$_2$F][OTf]$_3$ (**^{3}[Cu$_2$F]$^{3+}$**) was identified using single-crystal X-ray crystallography as the first structurally characterized example of a copper(II)-fluoride PDI complex (Figure 5). Unlike the monochloride species **^{3}[Cu$_2$Cl]$^{3+}$**, the dinuclear Cu$_2$F core is accom-

modated by an unfolded conformation of the macrocyclic ligand. The crystal structure also displays a linear arrangement of atoms within the macrocyclic pocket leading to a Cu-F-Cu angle of 180.00°. For the fluoride ligand to fit in this linear arrangement, the Cu–Cu distance increases to 3.7240(4) Å, a similar distance to ^{3}**[Cu$_2$Cl]$^{3+}$**. Each Cu(II) center is capped by a triflate anion (Cu–O distance of 2.2707(19) Å) and adopts a square pyramidal geometry (τ_5 = 0.03 for each Cu(II) center). A large thermal ellipsoid is present on the μ-F, indicating that the bridging fluoride unit is oscillating back and forth in the macrocyclic pocket. The short Cu–F bond length (1.8620(3) Å) agrees with the related four-coordinate pyridyldiamide copper(II)-fluoride complex reported by Zhang and coworkers (1.828(2) Å) [31,32].

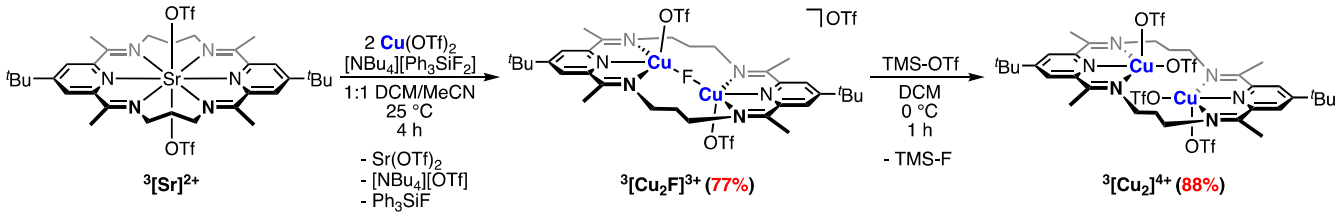

Scheme 3. Abstraction of bridging fluoride from ^{3}**[Cu$_2$F]$^{3+}$** using TMS-OTf in DCM.

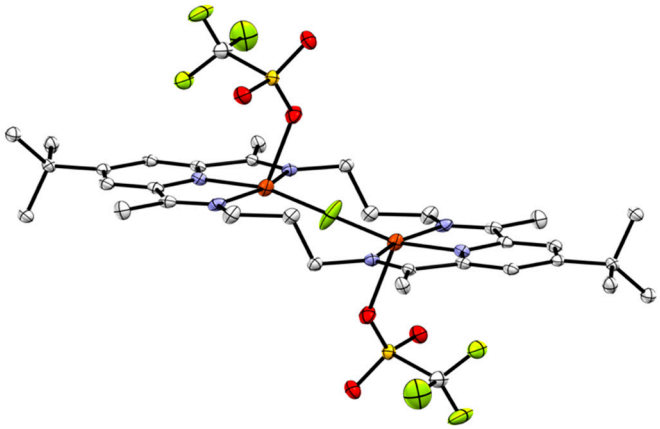

Figure 5. Crystal structure of ^{3}**[Cu$_2$F]$^{3+}$** (thermal ellipsoids set at 50% probability; hydrogen atoms, triflate disorder, and outer-sphere anions omitted for clarity). The following atoms shown in this figure are color-coded for convenience: Cu (orange), N (blue), C (light grey), F (yellow-green), S (yellow), and O (red).

The removal of the fluoride ligand using TMS-OTf was carried out in DCM at −78 °C. The dark blue slurry became light blue upon the slow addition of TMS-OTf. Combustion analysis supported the formation of the Cu$_2$(II,II) tetratriflate macrocyclic complex [(^{3}PDI$_2$)Cu$_2$][OTf]$_4$ (^{3}**[Cu$_2$]$^{4+}$**). The product, like ^{3}**[Cu$_2$(NCMe)$_2$]$^{4+}$**, was insoluble in common organic solvents, and, due to the increased insolubility, single crystals of the product remained elusive. However, based on the structural data obtained for ^{3}**[Cu$_2$Cl$_2$]$^{2+}$** and ^{3}**[Cu$_2$(NCMe)$_2$]$^{4+}$**, an unfolded ligand conformation is a reasonable assignment of the product's overall geometry, and considering the similarity in the colors of ^{3}**[Cu$_2$(NCMe)$_2$]$^{4+}$**, ^{3}**[Cu$_2$F]$^{3+}$**, and ^{3}**[Cu$_2$]$^{4+}$** as well as the low solubility of ^{3}**[Cu$_2$]$^{4+}$**, an ionic structure with five-coordinate Cu centers would be reasonable to propose. This formulation could be achieved through a number of combinations of triflate coordination mode, denticity, and ionicity. In the absence of further structural data, we have chosen to represent ^{3}**[Cu$_2$]$^{4+}$** with the generic structure shown in Scheme 3 while acknowledging that another formulation may well represent the structure of this species.

2.4. Anion Substitution Reactions with $^3[Cu_2]^{4+}$

2.4.1. Anion Substitution with Halides and Pseudohalides

To confirm the structure and assess anion binding within the macrocyclic pocket of ^{3}**[Cu$_2$]$^{4+}$**, the material was first treated with 2.0 equiv of NBu_4Cl to generate the previously isolated ^{3}**[Cu$_2$Cl$_2$]$^{2+}$** (Scheme 4, Top). As the reaction proceeded in MeCN, the insoluble blue ^{3}**[Cu$_2$]$^{4+}$** material was consumed. A sharp color change to dark green signified the conversion to the desired product. The solubility profile and color of the resulting product matched that of the independently synthesized ^{3}**[Cu$_2$Cl$_2$]$^{2+}$**, and both IR and UV-vis-NIR spectroscopic measurements confirmed the identity of the product as ^{3}**[Cu$_2$Cl$_2$]$^{2+}$**. Facile anion substitution demonstrated the enhanced reactivity of ^{3}**[Cu$_2$]$^{4+}$** compared to the more inert ^{3}**[Cu$_2$Cl$_2$]$^{2+}$**.

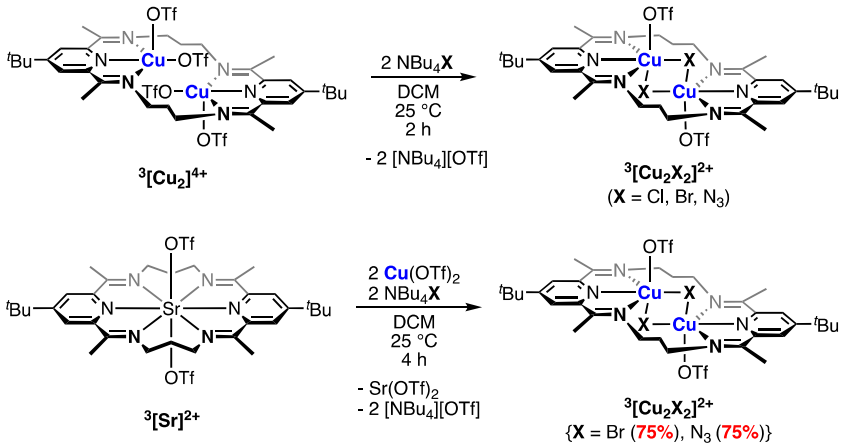

Scheme 4. Top: Anion metathesis with ^{3}**[Cu$_2$]$^{4+}$**. **Bottom**: One-pot anion metathesis with ^{3}**[Sr]$^{2+}$**.

The introduction of a new bridging group was achieved by treating ^{3}**[Cu$_2$]$^{4+}$** with 2.0 equiv NBu_4Br (Scheme 4, Top). Upon the addition of NBu_4Br to a blue MeCN slurry of ^{3}**[Cu$_2$]$^{4+}$**, a reaction was signified by a color change to green. After two hours of stirring, the solution appeared homogeneous. The product was obtained as a bright green powder. Attempts at the crystallization of the macrocyclic complex afforded powders. The identity of the product was confirmed through combustion analysis as the Cu_2-di(μ-Br) complex $[(^3PDI_2)Cu_2Br_2][OTf]_2$ (^{3}**[Cu$_2$Br$_2$]$^{2+}$**). The infrared spectrum displayed an imine stretching frequency at 1600 cm^{-1}. Further support for the dinuclear product was obtained through UV-vis-NIR spectroscopy. Absorption bands were identified at 236 nm ($\pi\rightarrow\pi^*$ transition) and 679 nm (d$\rightarrow$d transition), which agree well with ^{3}**[Cu$_2$Cl$_2$]**$^{2+}$.

The treatment of ^{3}**[Cu$_2$]$^{4+}$** with 2.0 equiv $[NBu_4][N_3]$ cleanly afforded the paramagnetic, dark green complex $[(^3PDI_2)Cu_2(N_3)_2][OTf]_2$ (^{3}**[Cu$_2$(N$_3$)$_2$]$^{2+}$**). Crystallization of the product allowed for structural elucidation (Figure 6). Two azide ligands now bridge the two copper(II) centers, while the macrocyclic ligand remains in the unfolded ligand conformation. Each Cu(II) center adopts a distorted octahedral geometry. The elongated Cu–N (2.5353(1) Å) and Cu–O (2.4361(9) Å) axial bond lengths are consistent with Cu-d^9 Jahn–Teller distortions. A symmetric $Cu_2(\mu\text{-}N_3)_2$ core is noted in the crystal structure, with a Cu–Cu distance of 3.1362(6) Å and symmetry-related Cu-N-Cu angles of 88.02(4)°. Although the Cu–Cu distance is similar to that in the analogous ^{3}**[Cu$_2$Cl$_2$]$^{2+}$** complex, the bridging angle observed for ^{3}**[Cu$_2$(N$_3$)$_2$]$^{2+}$** is larger, owing to the shorter equatorial Cu–N bond lengths of 1.936(1) Å. Further support for the di(μ-azide) core was noted in the compound's IR spectrum. An asymmetric azide stretching frequency was observed at 2062 cm^{-1}. Similar stretching frequencies have been observed in analogous Schiff base complexes [33–36].

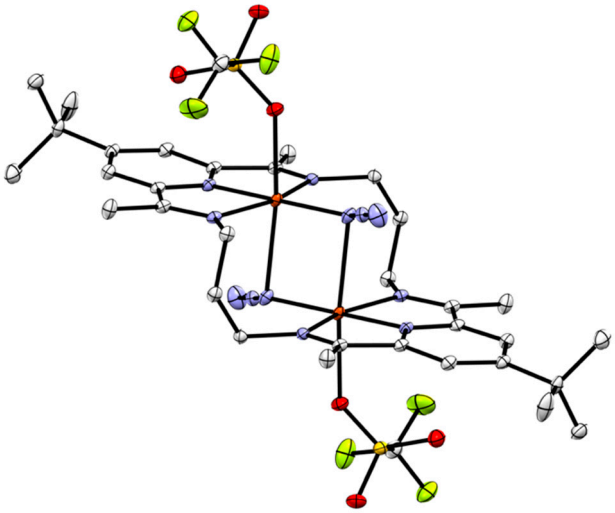

Figure 6. Crystal structure of ^{3}**[Cu$_2$(N$_3$)$_2$]$^{2+}$** (thermal ellipsoids set at 50% probability; hydrogen atoms omitted for clarity). The following atoms shown in this figure are color-coded for convenience: Cu (orange), N (blue), C (light grey), F (yellow-green), S (yellow), and O (red).

Considering the ease of anion substitution displayed by ^{3}**[Cu$_2$]$^{4+}$**, we pursued a simplified one-pot protocol for the synthesis of ^{3}**[Cu$_2$X$_2$]$^{2+}$** species (Scheme 4, Bottom). As noted above, treating ^{3}**[Sr]$^{2+}$** and 2.0 equiv Cu(OTf)$_2$ in DCM afforded no reaction. However, upon the addition of 2.0 equiv of NBu$_4$X (X = N$_3$, Br) to the mixture, an anion metathesis and macrocycle transmetallation reaction was initiated to yield the ^{3}**[Cu$_2$(μ-X)$_2$]$^{2+}$** products. These results indicate that anion metathesis is facile in this system and that the formation of ^{3}**[Cu$_2$]$^{4+}$** is not necessary prior to the generation of the ^{3}**[Cu$_2$(μ-X)$_2$]$^{2+}$** products. While this one-pot route afforded comparable yields to the stepwise procedure, the extended workup and separation of multiple salt byproducts proved more challenging. Anion metathesis studies with ^{3}**[Cu$_2$]$^{4+}$** were continued to avoid such difficulties.

2.4.2. Anion Substitution with Nitrite and Trimethylsilanolate Anions

We next pursued the inclusion of the nitrite anion, which is known to be capable of adopting a range of coordination modes at Cu(II) ions. To first probe if ^{3}**[Cu$_2$]$^{4+}$** was capable of binding nitrite, a similar protocol was followed as that described above, in which NaNO$_2$ was used in the anion metathesis reaction (Scheme 5). Upon adding 2.0 equiv of NaNO$_2$ to a slurry of ^{3}**[Cu$_2$]$^{4+}$**, the starting material was consumed over the course of 2 h to afford a dark blue-green solution. The diffusion of Et$_2$O into a concentrated MeCN solution afforded crystals suitable for X-ray diffraction. The product was identified as the di(μ-κ^1-ONO) macrocycle complex, [(^{3}PDI$_2$)Cu$_2$(ONO)$_2$][OTf]$_2$ (^{3}**[Cu$_2$(ONO)$_2$]$^{2+}$**).

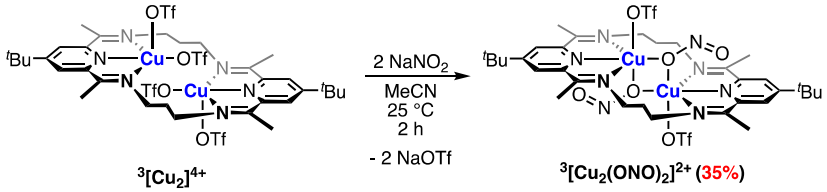

Scheme 5. Synthesis of ^{3}[Cu$_2$(ONO)$_2$]$^{2+}$ in MeCN.

The solid-state structure of ^{3}**[Cu$_2$(ONO)$_2$]$^{2+}$** depicts the macrocyclic ligand enforcing a μ-κ^1-binding of each nitrite anion (Figure 7). Limited examples of this geometry are found for Cu$_2$(II,II) systems in the literature [37–40]. In ^{3}**[Cu$_2$(ONO)$_2$]$^{2+}$**, each copper resides in a distorted octahedral geometry, with the overall structure appearing similar in form to ^{3}**[Cu$_2$(N$_3$)$_2$]$^{2+}$**. The two copper(II) centers are related by a center of symmetry in the crystal lattice and are separated by 3.2553(6) Å. The characteristic Cu(II)-d^9 Jahn–Teller distortions

are observed through the elongated Cu–O bond lengths (2.347(1) Å and 2.505(1) Å). Like ^{3}**[Cu$_2$(N$_3$)$_2$]$^{2+}$**, the Cu$_2$(ONO)$_2$ core displays a larger bridging angle (∠Cu-O-Cu = 94.18(5)°) than that observed in ^{3}**[Cu$_2$Cl$_2$]$^{2+}$**. The short equatorial Cu–O bond lengths of 1.904(1) Å account for this difference.

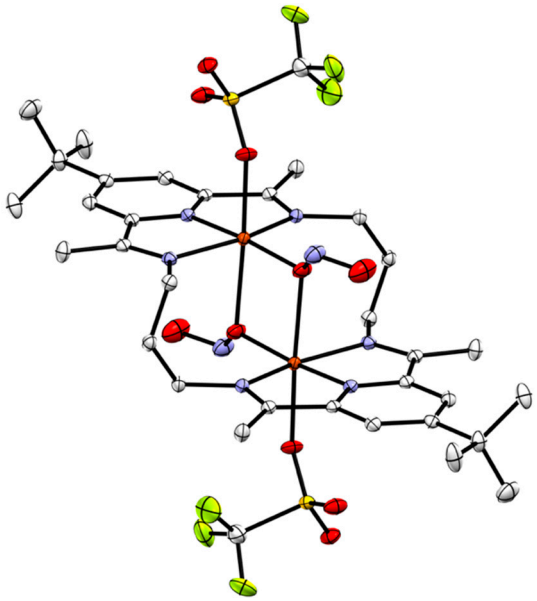

Figure 7. Crystal structure of ^{3}**[Cu$_2$(ONO)$_2$]$^{2+}$** (thermal ellipsoids set at 50% probability; hydrogen atoms and nitrite disorder omitted for clarity). The following atoms shown in this figure are color-coded for convenience: Cu (orange), N (blue), C (light grey), F (yellow-green), S (yellow), and O (red).

The IR spectral data for ^{3}**[Cu$_2$(ONO)$_2$]$^{2+}$** are consistent with the nitrite ligation mode observed crystallographically. IR spectra of Cu$_2$(II,II) complexes with κ^1-ONO ligands show asymmetric and symmetric stretching modes in the 1400–1100 cm^{-1} region [37,38]. However, the bending and stretching frequencies associated with the macrocyclic ligand convolute the IR spectrum of ^{3}**[Cu$_2$(ONO)$_2$]$^{2+}$**. To distinguish the nitrite stretching frequencies from the macrocyclic ligand, the isotopically labeled complex [(^{3}PDI$_2$)Cu$_2$(O^{15}NO)$_2$][OTf]$_2$ (^{3}**[Cu$_2$(O^{15}NO)$_2$]$^{2+}$**) was prepared. The IR spectrum of ^{3}**[Cu$_2$(ONO)$_2$]$^{2+}$** contains two distinct stretching frequencies at 1473 cm^{-1} and 991 cm^{-1} that shift to lower energies (1447 cm^{-1} and 971 cm^{-1}) when using ^{3}**[Cu$_2$(O^{15}NO)$_2$]$^{2+}$** (Figure 8). Thus, the stretching frequencies at 1473 cm^{-1} and 991 cm^{-1} are assigned to the asymmetric and symmetric stretching frequencies of the nitrite ligands.

Bridging alkoxy anions were next targeted as a way of expanding the scope of substitution reactions available to ^{3}**[Cu$_2$]$^{4+}$**, but Cu$_2$(II,II)-μ-(OR) (R = Me, ^{t}Bu, Ph) macrocyclic species eluded isolation. Instead, substitution was found to be successful when using the trimethylsilanolate anion (Scheme 6). Upon the addition of 2.0 equiv NaOTMS to a slurry of ^{3}**[Cu$_2$]$^{4+}$**, a rapid color change from blue to dark orange-brown was observed. Low-temperature crystallization afforded single crystals of the desired complex, [(^{3}PDI$_2$)Cu$_2$(OTMS)$_2$][OTf]$_2$ (^{3}**[Cu$_2$(OTMS)$_2$]$^{2+}$**). The crystal structure confirms the presence of two bridging trimethylsilanolate ligands (Figure 9). The ligand adopts an unfolded ligand conformation to support the two bridging ligands between the two copper(II) centers. In the case of ^{3}**[Cu$_2$(OTMS)$_2$]$^{2+}$**, both Cu(II) centers were found to adopt a distorted square pyramidal geometry with the triflate anions lying in the outer coordination sphere (τ_5 = 0.14 for each Cu(II)). The steric encumbrance of the TMS groups may prevent the triflate anions from binding to the metal centers in the manner seen with the structurally related complexes presented above.

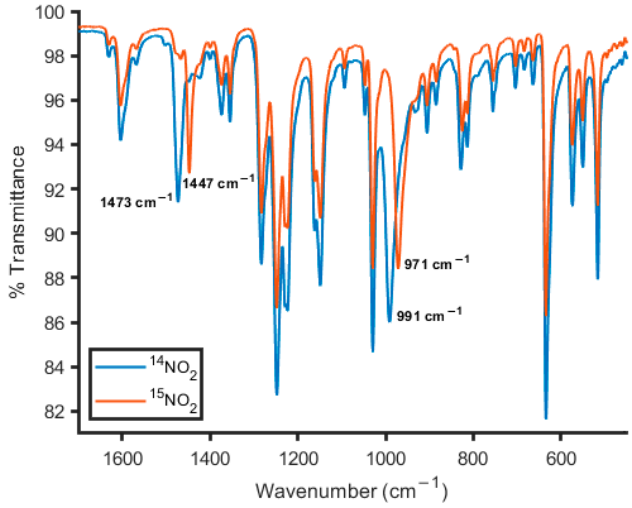

Figure 8. Overlay of infrared spectra of $^{3}[Cu_2(O^{14/15}NO)_2]^{2+}$.

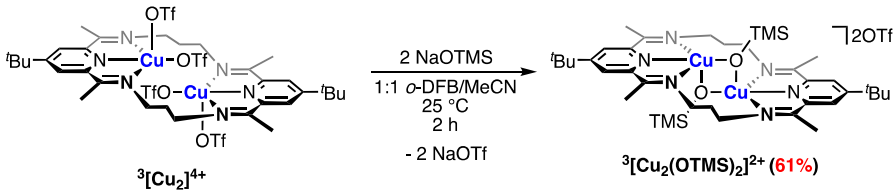

Scheme 6. Synthesis of $^{3}[Cu_2(OTMS)_2]^{2+}$ in *o*-DFB/MeCN.

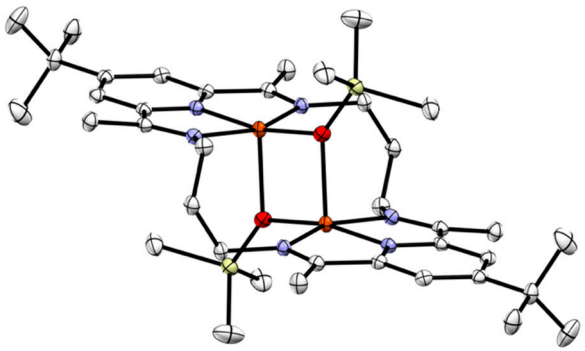

Figure 9. Crystal structure of $^{3}[Cu_2(OTMS)_2]^{2+}$ (thermal ellipsoids set at 50% probability; hydrogen atoms and outer-sphere anions omitted for clarity). The following atoms shown in this figure are color-coded for convenience: Cu (orange), N (blue), C (light grey), O (red), and Si (tan).

The $Cu_2(\mu$-OTMS$)_2$ diamond core displays a Cu-O-Cu angle of 86.65(5)°, an equatorial Cu–O bond length of 1.8969(14) Å, a distorted axial Cu–O bond length of 2.259(1) Å, and a short Cu–Cu distance of 2.8639(4) Å. To date, no structurally characterized Cu_2(II,II)-μ-OTMS complexes have been reported in the CSD. McGeary, Caulton, and coworkers previously reported a Cu_2(I,I)-*bis*(μ-$OSiPh_3$)-*bis*(diphenylmethylphosphine) cluster [41]. The cluster was found to contain an asymmetric $[Cu_2(OSiPh_3)_2]$ core, with longer Cu–O bond distances of 1.9457(17) and 2.0456(17) Å. The shorter equatorial bond distances observed in $^{3}[Cu_2(OTMS)_2]^{2+}$ are as expected, considering the higher oxidation states of the metal centers. A longer Cu–Cu distance of 2.9662(7) Å was also observed for the $[Cu_2(OSiPh_3)_2]$ cluster. Compared with $^{3}[Cu_2(OTMS)_2]^{2+}$, each copper center in McGeary and Caulton's cluster is more sterically crowded, owing to the bulky diphenylmethylphosphine ligand. The combined action of the lower oxidation states and increased steric bulk at the metal centers forces a farther copper–copper distance.

2.4.3. Synthesis of $^{3}[Cu_2OH]^{3+}$

The synthetic protocol for anion exchange with **$^{3}[Cu_2]^{4+}$** was lastly implemented with the hydroxide anion. Numerous Cu_2(II,II)-di(μ-OH)-containing complexes exist that are supported with mononucleating, multidentate ligands, such as BDI (BDI = β-diketiminate) [42], Tp^R (Tp = hydrotris(1-pyrazolyl)borate; R = Me, ^{i}Pr) [43,44], and TACN (TACN = 1,4,7-triazacyclononane) [45]. The isolation of a Cu_2(II,II)-di(μ-OH) complex with $^{3}PDI_2$ has remained elusive, but the monohydroxide product $[(^{3}PDI_2)Cu_2OH][OTf]_3$ (**$^{3}[Cu_2OH]^{3+}$**) was synthesized through a treatment of **$^{3}[Cu_2]^{4+}$** with LiOH (Scheme 7).

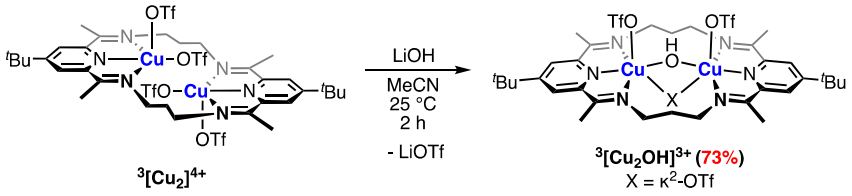

Scheme 7. Synthesis of **$^{3}[Cu_2OH]^{3+}$** in MeCN.

The growth of single crystals allowed for the structural elucidation of **$^{3}[Cu_2OH]^{3+}$**. The crystal structure was found to contain a planar macrocyclic ligand (Figure 10). Because of this conformation, the Cu–Cu distances lengthen to 3.585(7) Å and 3.618(4) Å (the asymmetric unit contains disordered macrocyclic complexes with distinct metrical parameters). These distances lie at the longer end of the range of Cu–Cu distances observed in the series of propylene-bridged *bis*(4-*tert*-butylpyridyldiimine) macrocyclic complexes. Each copper(II) center adopts a distorted octahedral geometry, with weakly coordinating triflate ligands occupying the axial positions of each copper(II) center. The PDI subunits and a bridging hydroxide ligand occupy the equatorial plane. The Cu–O(H) distances of 1.872(2) and 1.875(5) Å agree well with previously reported PDI_2-supported Cu_2(II,II)-μ-OH complexes (Table 2). However the Cu-O(H)-Cu angle of 149.98(16)° [140.2(2)°] significantly deviates from that of $[(^{Et}PDI_2)Cu_2OH][ClO_4]_3{\cdot}2H_2O$ [110.3(7)°]. The less-strained **$^{3}[Cu_2OH]^{3+}$** complex allows for the increased Cu–Cu distance and corresponding increase in the Cu-O(H)-Cu angle. In fact, the observed angle in **$^{3}[Cu_2OH]^{3+}$** agrees better with the larger complex $[(^{Oct}PDI_2)Cu_2OH][ClO_4]_3{\cdot}H_2O$ reported by Drew and Nelson [141.7(7)°]. As expected, the flexible aliphatic linkers modulate the Cu–Cu distance to allow for variously sized bridging ligands to be housed between the two metal centers.

Table 2. Selected bond metrics of copper(II) hydroxide PDI complexes.

	$^{3}[Cu_2OH]^{3+}$	**$[(^{Et}PDI_2)Cu_2OH]^{3+}$** [b,c]	**$[(^{Oct}PDI_2)Cu_2OH]^{3+}$** [c]
Cu(1)—N(1)/Å	2.097(2)	2.066(12)	2.039(11)
Cu(1)—N(2)/Å	1.912(2)	1.916(13)	1.907(16)
Cu(1)—N(3)/Å	2.040(3)	2.061(13)	2.060(9)
Cu(2)—N(4)/Å	2.096 [a]	-	2.076(4)
Cu(2)—N(5)/Å	1.926 [a]	-	1.925(12)
Cu(2)—N(6)/Å	2.038 [a]	-	2.059(14)
Cu(1)—O(1)/Å	1.872(2)	1.916(9)	1.866(13)
Cu(2)—O(1)/Å	1.908 [a]	-	1.912(10)
Cu(1)—Cu(2)/Å	3.603 [a]	3.145(4)	3.57
∠Cu(1)-O(1)-Cu(2)/°	145.09 [a]	110.3(7)	141.7(7)
Δ/Å	0.196 [a]	0.230	0.147

[a] Average values based on disorder of molecule. [b] Macrocycle is symmetric; bond metrics are the same for Cu(2). [c] Crystal structure obtained at room temperature.

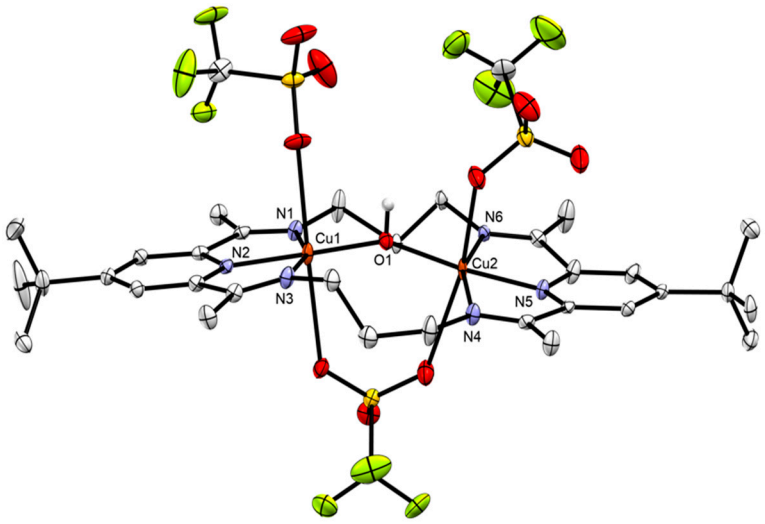

Figure 10. Crystal structure of ^{3}**[Cu$_2$OH]$^{3+}$** (thermal ellipsoids set at 50% probability; hydrogen atoms, solvent molecules, triflate disorder, and macrocycle disorder omitted for clarity). The following atoms shown in this figure are color-coded for convenience: Cu (orange), N (blue), C (light grey), F (yellow-green), S (yellow), O (red), and H (light grey, no octant).

3. Materials and Methods

3.1. General Considerations

Unless stated otherwise, all reactions were carried out under an inert atmosphere of N_2 using standard Schlenk techniques or a PureLab HE glovebox then worked up in air. Glassware, stir bars, filter aid (Celite), and 4 Å molecular sieves were dried in an oven at 175 °C for at least one hour prior to use when applicable. Degassed anhydrous solvents (Pentane, Et_2O, THF, DCM, and MeCN) were dried via passage through activated alumina using a Solvent Purification System and stored over 4 Å molecular sieves for at least one day before use. Chloroform-*d* was purchased from Cambridge Isotopes Laboratories, Inc., and was stored over 4 Å molecular sieves for at least one day before use. The macrocyclic precursor **^{2}[Sr]$^{2+}$** was prepared according to a previous reported procedure [46]. Tetrabutylammonium chloride (NBu_4Cl) was purchased from Sigma Aldrich, Saint Louis, MO, USA, ground to a fine powder with a mortar and pestle, then dried under vacuum over P_2O_5 for one week before use. Tetrabutylammonium bromide (NBu_4Br) was purchased from Sigma Aldrich and dried under vacuum over P_2O_5 for one week before use. Sodium nitrite ($NaNO_2$) was purchased from Fisher Chemicals, Whippany, NJ, USA, ground to a fine powder with a mortar and pestle, and flame dried under dynamic vacuum, then it was stored under N_2 in an inert atmosphere glovebox. ^{15}N-labeled sodium nitrite ($Na^{15}NO_2$) was purchased from Cambridge Isotope Laboratories, Inc., Andover, MA, USA, ground to a fine powder with a mortar and pestle, and flame dried under dynamic vacuum. The isotopologue was then stored in the dark, in the glovebox. Sodium trimethylsilanolate was purchased as a 1.0 M solution in THF from Sigma Aldrich in a Sure/Seal^{TM} bottle and was stored under N_2 in the glovebox. All other reagents were purchased from commercial vendors and used as received.

NMR spectroscopy: NMR spectra were recorded on a Bruker NEO 600 spectrometer. All chemical shifts are reported in units of ppm and referenced to the residual proteo-solvent resonance for proton and carbon chemical shifts. Internal $PhCF_3$ was used for referencing the ^{19}F spectrum [47].

Elemental analysis: Analytical data were obtained from the CENTC Elemental Analysis Facility at the University of Rochester. Microanalysis samples were weighed with a PerkinElmer Model AD6000 Autobalance and their compositions were determined with a PerkinElmer 2400 Series II Analyzer. Air-sensitive samples were handled in a VAC Atmospheres glovebox and combusted in a tin capsule that was crimp-sealed with a die

apparatus. For ^{3}**[Cu$_2$(NCMe)$_2$]$^{2+}$**, analytical data were collected using a Costech ECS 4010 analyzer in the Earth & Environmental Science Department at the University of Pennsylvania.

Infrared spectroscopy: Infrared spectra were recorded using a PerkinElmer Spectrum Two FT-IR spectrometer. Samples were placed on an ATR crystal after collecting a blank spectrum and spectral data were measured over the range of 450–4000 cm^{-1}. Samples requiring a KBr pellet were analyzed using a Bruker Invenio-R FT-IR spectrometer and spectral data were measured over the range of 450–4000 cm^{-1}.

UV-vis-NIR spectroscopy: Absorption spectra were collected over the range of 200–1000 nm using an Agilent Cary 60 UV-vis-NIR spectrophotometer. Stock solutions (3.0–11.0 mM) were prepared under a N_2 atmosphere in the glovebox. Samples were then diluted to obtain absorption profiles in the linear response range of the spectrophotometer. Each measurement was obtained using a 10 mm path-length quartz cuvette with a screw cap. The temperature of each measurement was maintained at 25 °C using an Unisoku USP-203A cryostat. Five different concentrations were used for Beer's Law analysis of each peak maxima. The absorption intensities for peak maxima were plotted vs. concentration to ensure a linear fit was obtained ($R^2 > 0.990$).

X-ray crystallography: X-ray intensity data were collected on a Bruker D8Quest CMOS (^{3}**[Cu$_2$Cl$_2$]$^{2+}$**, ^{2}**[Cu$_2$Cl$_2$]$^{2+}$**, and ^{3}**[Cu$_2$OH]$^{3+}$**) and a Bruker APEXII CCD (^{3}**[Cu$_2$(OTMS)$_2$]$^{2+}$**) area detector diffractometer with graphite-monochromated Mo-Kα radiation (λ = 0.71073 Å) at a temperature of 100 K. X-ray intensity data for ^{3}**[Cu$_2$Cl]$^{3+}$**, ^{3}**[Cu$_2$F]$^{3+}$**, and ^{3}**[Cu$_2$(ONO)$_2$]$^{2+}$** were collected on a Rigaku XtaLAB Synergy-S diffractometer equipped with an HPC area detector (Dectris Pilatus3 R 200K) employing confocal multilayer optic-monochromated Mo-Kα radiation (λ = 0.71073 Å) at a temperature of 100 K. X-ray intensity data for ^{3}**[Cu$_2$(N$_3$)$_2$]$^{2+}$** and ^{3}**[Cu$_2$(NCMe)$_2$]$^{3+}$** were collected on a Rigaku XtaLab Synergy-S diffractometer equipped with an HPC area detector (HyPix-6000HE) employing confocal multilayer optic-monochromated Mo-Kα radiation (λ = 0.71073 Å) (^{3}**[Cu$_2$(N$_3$)$_2$]$^{2+}$**) or Cu-Kα radiation (λ = 1.54184 Å) (^{3}**[Cu$_2$(NCMe)$_2$]$^{3+}$**) at a temperature of 100 K. Rotation frames were integrated using SAINT or CrysAlisPro, producing a listing of unaveraged F^2 and σ(F^2) values. The intensity data were corrected for Lorentz and polarization effects and for absorption using SADABS or SCALE3 ABSPACK. The structures were solved by direct methods using either SHELXT (^{3}**[Cu$_2$Cl$_2$]$^{2+}$**, ^{2}**[Cu$_2$Cl$_2$]$^{2+}$**, ^{3}**[Cu$_2$(NCMe)$_2$]$^{3+}$**, ^{3}**[Cu$_2$F]$^{3+}$**, ^{3}**[Cu$_2$(N$_3$)$_2$]$^{2+}$**, ^{3}**[Cu$_2$(ONO)$_2$]$^{2+}$**, and ^{3}**[Cu$_2$OH]$^{3+}$**) or SHELXS-97 (^{3}**[Cu$_2$(OTMS)$_2$]$^{2+}$**) and refined by full-matrix least-squares, based on F^2, using SHELXL-2018. All reflections were used during refinement. Non-hydrogen atoms were refined anisotropically, and hydrogen atoms were refined using a riding model. For ^{3}**[Cu$_2$Cl$_2$]$^{2+}$ and ^{3}[Cu$_2$(N$_3$)$_2$]$^{2+}$**, the molecule lies on a crystallographic center of symmetry (at $\frac{1}{2}$, $\frac{1}{2}$, $\frac{1}{2}$). For ^{3}**[Cu$_2$(ONO)$_2$]$^{2+}$**, the coordinate NO_2 is disordered by a slight rotation about the Cu1-O1 bond with relative occupancies of 0.72/0.28. For ^{3}**[Cu$_2$(OTMS)$_2$]$^{2+}$**, the molecule lies on a crystallographic center of symmetry (at 0, 0, 0). CCDC entries 2,284,784–2,284,792 contain the supplementary crystallographic data for this paper. These data can be obtained free of charge via http://www.ccdc.cam.ac.uk/conts/retrieving.html (accessed on 19 August 2023) (or from the CCDC, 12 Union Road, Cambridge CB2 1EZ, UK; Fax: +44 1223 336033; E-mail: deposit@ccdc.cam.ac.uk).

3.2. Synthetic Procedures

^{3}**[Sr]$^{2+}$**. The following procedure was adapted from the literature report [46]. A 500 mL round-bottom flask was charged with 4-*tert*-butyl-2,6-diacetylpyridine (5.1349 g, 23.417 mmol, 2.00 equiv), Sr(OTf)$_2$ (4.5353 g, 11.757 mmol, 1.00 equiv), and MeOH (250 mL). The mixture was stirred until all solids were dissolved. To the pale-yellow solution, 1,3-diaminopropane (2.00 mL, 23.9 mmol, 2.04 Eq.) was added. The solution became darker and was heated to reflux (oil bath set to 75 °C) for 16 h. The volatile materials were then removed under vacuum. The crude product was extracted into ca. 25 mL DCM and filtered over a pad of celite to remove insoluble materials. The yellow-orange filtrate was then

treated with ca. 300–400 mL hexanes to precipitate the product as an off-white powder. The powder was collected via vacuum filtration, washed with an additional ca. 500 mL hexanes, and dried under vacuum (9.6398 g, 91%). Analytical characterization data matched those previously reported. **^{1}H NMR** ($CDCl_3$, 600 MHz, 298 K): δ = 7.81 (s, 8H), 3.96 (t, *J* = 6.5 Hz, 8H), 2.46 (s, 12 H), 1.90 (quint, *J* = 6.5 Hz, 4H), 1.43 (s, 18H) ppm. **^{13}C{^{1}H} NMR** ($CDCl_3$, 151 MHz, 298 K): δ = 167.1, 164.0, 155.6, 121.4, 120.1 (q, *J* = 319.4 Hz), 46.7, 35.5, 30.67, 28.9, 15.2 ppm. **^{19}F{^{1}H} NMR** ($CDCl_3$, 565 MHz, 298 K): δ = −78.06 ppm.

^{3}[Cu$_2$Cl$_2$]$^{2+}$. The following procedure was carried out in air. A 100 mL round-bottom flask was charged with **^{3}[Sr]$^{2+}$** (553.4 mg, 0.6145 mmol, 1.00 equiv) and MeOH (15 mL). Once all starting material was dissolved, the golden-yellow solution was treated with a solution of $CuCl_2 \cdot 2H_2O$ (209.8 mg, 1.231 mmol, 2.00 equiv) in MeOH (10 mL). The reaction mixture immediately became dark green and was stirred for 60 min at room temperature. The solvent was then removed under vacuum. The product was extracted in 20 mL MeCN and filtered over a pad of Celite to remove insoluble byproducts. The dark blue-green filtrate was then layered with 80 mL Et_2O at room temperature. After one day, a crystalline solid was collected via vacuum filtration and rinsed with 50 mL Et_2O. The product was collected as a blue powder and dried under vacuum (517.0 mg, 83%). Crystals suitable for single-crystal X-ray crystallography were grown via the slow diffusion of Et_2O into a concentrated MeCN solution at room temperature. **Anal. % Calcd.** for $C_{34}H_{46}Cl_2Cu_2F_6N_6O_6S_2$ (1010.88 g/mol): C, 40.40; H, 4.59; N, 8.31. Found: C, 40.06; H, 4.51 N, 8.22. **FT-IR** (ATR): 1597 (C=N) cm^{-1}. **UV-vis-NIR** (MeCN, 298 K): 238 nm (7.71×10^4 M^{-1} cm^{-1}), 676 nm (242 M^{-1} cm^{-1}).

^{2}[Cu$_2$Cl$_2$]$^{2+}$. The following procedure was carried out in air. A 100 mL round-bottom flask was charged with **^{2}[Sr]$^{2+}$** (520.9 mg, 0.5969 mmol, 1.00 equiv) and MeOH (15 mL). Once all starting material was dissolved, the golden-yellow solution was treated with a solution of $CuCl_2 \cdot 2H_2O$ (206.9 mg, 1.214 mmol, 2.03 equiv) in MeOH (10 mL). The reaction mixture immediately became dark green and was stirred for 60 min at room temperature. The solvent was then removed under vacuum. The product was extracted in ca. 20 mL MeCN and filtered over a pad of celite to remove insoluble byproducts. The dark blue-green filtrate was then layered with ca. 80 mL Et_2O at room temperature. After one day, a crystalline solid was collected via vacuum filtration and rinsed with 50 mL Et_2O. The product was collected as a blue powder and dried under vacuum (481.1 mg, 82%). Crystals suitable for single-crystal X-ray crystallography were grown via the slow diffusion of Et_2O into a concentrated MeCN solution at room temperature. **Anal. % Calcd.** For $C_{32}H_{42}Cl_2Cu_2F_6N_6O_6S_2$ (982.83 g/mol): C, 39.11; H, 4.31; N, 8.55. Found: C, 38.89; H, 4.19; N, 8.44. **FT-IR** (ATR): 1594 (C=N) cm^{-1}. **UV-vis-NIR** (MeCN, 298 K): 236 nm (5.31×10^4 M^{-1} cm^{-1}), 681 nm (228 M^{-1} cm^{-1}).

^{3}[Cu$_2$(NCMe)$_2$]$^{4+}$. To a 100 mL Schlenk tube, **^{3}[Cu$_2$Cl$_2$]$^{2+}$** (1.094 g, 1.082 mmol, 1.00 equiv) and MeCN (24 mL) were added. Once all solids were dissolved, the stirred, dark green solution was cooled to 0 °C and treated dropwise with TMS-OTf (0.790 mL, 4.37 mmol, 4.04 equiv). The solution immediately turned dark blue and was warmed to room temperature over 30 min. The solvent was then removed under vacuum. The crude product was triturated with ca. 25 mL Et_2O and concentrated under vacuum to afford a light blue solid. The solid was transferred to the glovebox, collected on a fritted glass filter, and washed with 4 x ca. 10 mL 1:1 MeCN/Et_2O followed by ca. 50 mL Et_2O. The product was then dried under vacuum. The resulting fine blue powder (1.232 g, 86%) was stored at −35 °C in a glovebox. A sample suitable for X-ray crystallography was grown via the slow diffusion of Et_2O into a concentrated MeCN solution at room temperature. From the same batch of isolated material, single crystals of **^{3}[Cu$_2$Cl]$^{3+}$** were grown via the slow diffusion of *n*-hexane into a concentrated *o*-F_2-C_6H_4 solution at room temperature. **Anal. % Calcd.** for $C_{40}H_{52}N_8Cu_2F_{12}O_{12}S_4$ (1320.21 g/mol): C, 36.39; H, 3.97; N, 8.49. Found: C, 36.29; H, 4.05; N, 8.70. **FT-IR** (KBr): 1599 (C=N), 2307, 2279, 2259 (C≡N) cm^{-1},

^{3}[Cu$_2$F]$^{3+}$. A 500 mL round-bottom Schlenk flask was charged with $Cu(OTf)_2$ (3.2736 g, 9.0513 mmol, 2.05 equiv) and DCM (40 mL). The slurry was stirred and treated with a

solution of ^{3}**[Sr]**$^{2+}$ (3.9844 g, 4.4246 mmol, 1.00 equiv) in DCM (40 mL) followed by a solution of [NBu_4][Ph_3SiF_2] (2.6507 g, 4.9099 mmol, 1.11 equiv) in MeCN (80 mL). The reaction mixture became dark blue and was stirred for 4 h at room temperature. The solution was filtered through a pad of Celite to remove insoluble materials. The Celite pad was rinsed with an additional 40 mL of 1:1 DCM:MeCN. The dark blue filtrate was then concentrated under vacuum to afford a crude blue oil, which solidified upon standing. The flask was transferred to the glovebox. The crude blue solid was washed with 3 × 30 mL 2:1 Et_2O:THF and collected over a fritted glass filter. The solid was washed with copious amounts of Et_2O followed by 3 × 25 mL THF (a dark impurity was removed). The remaining crystalline blue solid was rinsed with ca. 50–60 mL pentane and dried under vacuum to afford the desired product (3.7947 g, 77%). Crystals suitable for single-crystal X-ray crystallography were grown by layering a concentrated MeCN solution with Et_2O at room temperature and letting the two layers diffuse together overnight. **Anal**. **% Calcd.** for $C_{35}H_{46}Cu_2F_{10}N_6O_9S_3$ (1108.04 g/mol): C, 37.94; H, 4.18; N, 7.58. Found: C, 37.88; H, 4.16; N, 7.58. **FT-IR** (ATR): 1589 (C=N) cm^{-1}. **UV-vis-NIR** (MeCN, 298 K): 230 nm, 667 nm (248 M^{-1} cm^{-1}).

^{3}**[Cu_2]**$^{4+}$. To a 100 mL Schlenk tube, ^{3}**[Cu_2F]**$^{3+}$ (1.1099 g, 1.0017 mmol, 1.00 equiv) and DCM (25 mL) were added. The blue slurry was cooled to −78 °C and treated dropwise with TMS-OTf (0.200 mL, 1.11 mmol, 1.10 equiv). The mixture was removed from the cold bath and stirred for one hour. Over time, the dark blue slurry became light blue. The solvent was then removed under vacuum affording a light blue solid. The solid was transferred to the glovebox, triturated with ca. 100–200 mL Et_2O, and collected via vacuum filtration. The product was then washed with ca. 100–200 mL pentane and dried under vacuum (1.0966 mg, 88%). **Anal**. **% Calcd.** for $C_{36}H_{46}Cu_2F_{12}N_6O_{12}S_4$ (1238.11 g/mol): C, 34.92; H, 3.75; N, 6.79. Found: C, 34.09; H, 3.53; N, 6.58. **FT-IR** (KBr): 1602 (C=N) cm^{-1}.

^{3}**[Cu_2Br_2]**$^{2+}$. To a 100 mL Schlenk tube, $Cu(OTf)_2$ (433.2 mg, 1.198 mmol, 2.04 Eq.) and DCM (5 mL) were added. The slurry was treated with a solution of ^{3}**[Sr]**$^{2+}$ (529.2 mg, 0.5877 mmol, 1.00 equiv) in DCM (10 mL). No change occurred upon this addition. A solution of NBu_4Br (379.4 mg, 1.177 mmol, 2.00 equiv) in DCM (10 mL) was then added. The reaction mixture immediately became dark green. Within minutes, a bright green solid precipitated from solution. The reaction was allowed to proceed for 4 h at room temperature. To the solution, MeCN (35 mL) was added, and the dark green solution was filtered over a pad of celite. The pad was rinsed with an additional 35 mL 1:1 DCM:MeCN, and the filtrate was concentrated under vacuum. The resulting crude solid was triturated with 10 mL THF and collected via vacuum filtration. The product was washed with 3 × 10 mL THF and 50 mL Et_2O. The product was re-dissolved in ca. 45 mL MeCN and was layered with 200 mL Et_2O at room temperature. The product powdered out of solution as a light green solid after three days. The solid was collected and rinsed with 50 mL Et_2O before drying under vacuum (487.2 mg, 75%). **Anal**. **% Calcd.** for $C_{34}H_{46}Br_2Cu_2F_6N_6O_6S_2$ (1099.79 g/mol): C, 37.13; H, 4.22; N, 7.64. Found: C, 37.12; H, 4.04; N, 7.57. **FT-IR** (ATR): 1600 (C=N) cm^{-1}. **UV-vis-NIR** (MeCN, 298 K): 236 nm, 679 nm (217 M^{-1} cm^{-1}).

^{3}**[$Cu_2(N_3)_2$]**$^{2+}$. To a 100 mL Schlenk tube, $Cu(OTf)_2$ (406.2 mg, 1.123 mmol, 2.02 equiv) and DCM (5 mL) were added. The slurry was treated with a solution of ^{3}**[Sr]**$^{2+}$ (501.1 mg, 0.5565 mmol, 1.00 equiv) in DCM (10 mL). No change occurred upon this addition. A solution of NBu_4N_3 (320.2 mg, 1.126 mmol, 2.02 equiv) in DCM (10 mL) was then added. The reaction mixture immediately became dark green. Within minutes, a dark green solid precipitated from solution. The reaction was allowed to proceed for 4 h at room temperature. To the solution, MeCN (25 mL) was added, and the dark green solution was filtered over a pad of celite. The pad was rinsed with an additional 35 mL 1:1 DCM/MeCN, and the filtrate was concentrated under vacuum. The resulting crude solid was triturated with 10 mL THF and collected via vacuum filtration. The product was washed with 3 × 10 mL THF and 50 mL Et_2O. The product was re-dissolved in ca. 45 mL MeCN and was layered with 200 mL Et_2O at room temperature. The product crystallized as green needles after three days. The crystals were collected and rinsed with 50 mL Et_2O before drying under

vacuum (424.7 mg, 75%). Crystals suitable for single-crystal X-ray crystallography were grown via the vapor diffusion of Et_2O into a concentrated MeCN solution. **Anal**. **% Calcd.** for $C_{34}H_{46}Cu_2F_6N_{12}O_6S_2$ (1024.02 g/mol): C, 39.88; H, 4.53; N, 16.41. Found: C, 39.91; H, 4.38; N, 16.25. **FT-IR** (ATR): 2063 (N_3), 1602 (C=N) cm^{-1}. **UV-vis-NIR** (MeCN, 298 K): 229 nm, 661 nm (418 M^{-1} cm^{-1}).

^{3}[Cu$_2$(ONO)$_2$]$^{2+}$. In a glovebox, a 20 mL scintillation vial was charged with **^{3}[Cu$_2$]$^{4+}$** (203.9 mg, 0.1647 mmol, 1.00 equiv), $NaNO_2$ (24.0 mg, 0.348 mmol, 2.11 equiv), and MeCN (ca. 8 mL). The blue slurry was stirred for 2 h at room temperature, at which point the dark blue-green solution appeared homogeneous. The sample was removed from the glovebox and worked up under air. The crude reaction mixture was diluted with DCM (10 mL) and filtered through a pad of celite to remove insoluble materials. The solvent was then removed under vacuum. The crude dark green solid was washed with 3 × 5 mL THF. A blue crystalline solid was collected via vacuum filtration and dried under vacuum to afford the desired product (59.5 mg, 35%). Crystals suitable for single-crystal X-ray crystallography were grown via the vapor diffusion of Et_2O into a concentrated MeCN solution. **Anal**. **% Calcd**. for $C_{34}H_{46}Cu_2F_6N_8O_{10}S_2$ (1031.99 g/mol): C, 39.57; H, 4.49; N, 10.86. Found: C, 39.61; H, 4.45; N, 10.72. **FT-IR** (ATR): 1603 (C=N), 1473, 991 (NO_2) cm^{-1}. **UV-vis-NIR** (MeCN, 298 K): 230 nm, 638 nm (248 M^{-1} cm^{-1}).

^{3}[Cu$_2$(O^{15}NO)$_2$]$^{2+}$. In the glovebox, a 20 mL scintillation vial was charged with **^{3}[Cu$_2$]$^{4+}$** (207.8 mg, 0.1678 mmol, 1.00 equiv), $Na^{15}NO_2$ (24.6 mg, 0.351 mmol, 2.09 equiv), and MeCN (ca. 8 mL). The blue slurry was stirred for 2 h at room temperature, at which point the dark blue-green solution appeared homogeneous. The sample was removed from the glovebox and worked up in air. The crude reaction mixture was diluted with DCM (10 mL) and filtered over a pad of celite to remove insoluble materials. The solvent was then removed under vacuum. The crude dark green solid was washed with 3 × ca. 2 mL THF. A blue-green powder was collected via vacuum filtration and dried under vacuum to afford the desired product (136.5 mg, 79%). **FT-IR** (ATR): 1604 (C=N), 1447, 971 (NO_2) cm^{-1}.

^{3}[Cu$_2$(OTMS)$_2$]$^{2+}$. In the glovebox, a 20 mL scintillation vial was charged with **^{3}[Cu$_2$]$^{4+}$** (211.4 mg, 0.1707 mmol, 1.00 equiv), *o*-DFB (ca. 5 mL), and MeCN (ca. 5 mL). The blue slurry was stirred at room temperature and treated dropwise with 1.0 M NaOTMS (0.350 mL, 0.350 mmol, 2.05 equiv). The reaction mixture quickly became dark orange-brown and was stirred for 2 h. The mixture was then directly filtered over a pad of celite, and the dark orange filtrate was concentrated under vacuum. The crude product was triturated with 3 × ca. 2–3 mL THF. The remaining dark blue-green solid was dissolved in minimal MeCN and filtered over celite. The sample was concentrated under vacuum, triturated with ca. 15 mL Et_2O, and dried under vacuum (116.7 mg, 61%). Crystals suitable for single-crystal X-ray crystallography were grown via the vapor diffusion of Et_2O into a concentrated MeCN solution at −35 °C. **Anal**. **% Calcd**. for $C_{40}H_{64}Cu_2F_6N_6O_8S_2Si_2$ (1118.36 g/mol): C, 42.96; H, 5.77; N, 7.51. Found: C, 42.89; H, 5.57; N, 7.80. **FT-IR** (ATR): 1603 (C=N) cm^{-1}. **UV-vis-NIR** (MeCN, 298 K): 229 nm, 481 nm (382 M^{-1} cm^{-1}).

^{3}[Cu$_2$OH]$^{3+}$. In the glovebox, a 20 mL scintillation vial was charged with **^{3}[Cu$_2$]$^{4+}$** (208.1 mg, 0.1681 mmol, 1.00 Eq.), LiOH (4.0 mg, 0.17 mmol, 0.99 Eq.), and MeCN (ca. 8 mL). The blue slurry was stirred at room temperature for 2 h, at which point the dark blue solution appeared homogeneous. The sample was removed from the glovebox and worked up in air. The solvent was removed under vacuum. The product was extracted in ca. 5 mL DCM and filtered over celite to remove insoluble materials. The dark blue filtrate was layered with ca. 15 mL hexanes. After one day, a blue crystalline solid was isolated and dried under vacuum (134.8 mg, 73%). Crystals suitable for single-crystal X-ray crystallography were grown via the vapor diffusion of Et_2O into a concentrated THF solution. **Anal**. **% Calcd**. for $C_{35}H_{47}Cu_2F_9N_6O_{10}S_3 \bullet 0.5\ CH_2Cl_2$ (1106.05 g/mol): C, 37.13; H, 4.21; N, 7.32. Found: C, 37.39; H, 4.33; N, 7.41. **FT-IR** (KBr): 1599 (C=N) cm^{-1}. **UV-vis-NIR** (MeCN, 298 K): 229 nm, 708 nm (246 M^{-1} cm^{-1}).

4. Conclusions

The research described in this manuscript enables a broad range of functionalization chemistry at a dicopper core supported by a geometrically and electronically flexible macrocyclic ligand. The isolation and characterization of this new series of Cu_2(II,II) *bis*(4-*tert*-butylpyridyldiimine) macrocycle complexes were carried out through three general procedures: (1) the transmetallation of ^{n}**[Sr]**$^{2+}$ with $CuCl_2$, (2) salt metathesis at a new "open-core" macrocycle, ^{3}**[Cu$_2$]**$^{4+}$, and (3) a one-pot procedure in which ^{3}**[Sr]**$^{2+}$ was treated with 2.0 equiv $Cu(OTf)_2$ and a corresponding source of anion. These methods were found to be suitable for accessing a host of novel Cu_2(II,II) macrocycles. Notably, previous work on the parent form of this macrocycle encountered persistent difficulties with solubility, hindering structural characterizations and further synthetic investigations. The improved solubility on the introduction of 4-*tert*-butylpyridyl groups and triflate counterions allowed for modest-to-good solubility profiles across a broad range of core substitutions.

The solid-state structures of each new macrocycle-supported complex revealed how the conformation of the macrocycle was able to change depending on the number and nature of bridging substituents between the Cu(II) centers (Table 3). If two bridging ligands are present, the macrocycle can adopt a range of ligand conformations to support the Cu_2X_2 cores, and, at its extreme, the macrocycle was found to unfurl into a nearly planar geometry to support a linear Cu_2F core. The geometric differences enabled by the flexibility of the macrocycles' aliphatic linkers were originally proposed by Drew and Nelson, but their data were limited by the solubility problems mentioned above. The present range of structural data highlights the flexibility of this ligand class. This flexibility, in combination with the robust synthetic protocols, provides an ideal platform for future investigations into the ability of these complexes to mediate small molecule activation and strong bond functionalization chemistry.

Table 3. Summary of Cu_2(II,II) *bis*(4-*tert*-butylpyridyldiimine) macrocycles.

	Conformation	Cu-Cu/Å	Cu-X$_{equatorial}$/Å [a]	Cu-X-Cu/° [a]
^{3}**[Cu$_2$Cl]**$^{2+}$	Unfolded	3.129(1)	2.1860	75.05
^{2}**[Cu$_2$Cl]**$^{2+}$	Unfolded	2.9922 [a]	2.2056	70.82
^{3}**[Cu$_2$(NCMe)$_2$]**$^{4+}$	Unfolded	3.3479(7)	1.973	77.64
^{3}**[Cu$_2$Cl]**$^{3+}$	Arched	3.7045(7)	2.2823	108.50
^{3}**[Cu$_2$F]**$^{3+}$	Unfolded	3.7240(4)	1.8620	180.00
^{3}**[Cu$_2$(N$_3$)$_2$]**$^{2+}$	Unfolded	3.1362(6)	1.936	88.02
^{3}**[Cu$_2$(ONO)$_2$]**$^{2+}$	Unfolded	3.2553(6)	1.904	94.18
^{3}**[Cu$_2$(OTMS)$_2$]**$^{2+}$	Unfolded	2.8639(4)	1.8969	86.65
^{3}**[Cu$_2$OH]**$^{3+}$	Planar	3.603 [a]	1.890	145.09

[a] Average values.

Supplementary Materials: The following supporting information can be downloaded at: https://www.mdpi.com/article/10.3390/inorganics11090348/s1, Figures S1–S3: NMR spectra of ^{3}**[Sr]**$^{2+}$; Figures S4–S14: IR spectra of ^{3}**[Cu$_2$Cl$_2$]**$^{2+}$, ^{2}**[Cu$_2$Cl$_2$]**$^{2+}$, ^{3}**[Cu$_2$(NCMe)$_2$]**$^{4+}$, ^{3}**[Cu$_2$]**$^{4+}$, ^{3}**[Cu$_2$F]**$^{3+}$, ^{3}**[Cu$_2$Br$_2$]**$^{2+}$, ^{3}**[Cu$_2$(N$_3$)$_2$]**$^{2+}$, ^{3}**[Cu$_2$(ONO)$_2$]**$^{2+}$, ^{3}**[Cu$_2$(O^{15}NO)$_2$]**$^{2+}$, ^{3}**[Cu$_2$(OTMS)$_2$]**$^{2+}$, and ^{3}**[Cu$_2$OH]**$^{3+}$; Figures S15–S40: UV-vis-NIR data for ^{3}**[Cu$_2$Cl$_2$]**$^{2+}$, ^{2}**[Cu$_2$Cl$_2$]**$^{2+}$, ^{3}**[Cu$_2$F]**$^{3+}$, ^{3}**[Cu$_2$(N$_3$)$_2$]**$^{2+}$, ^{3}**[Cu$_2$(ONO)$_2$]**$^{2+}$, ^{3}**[Cu$_2$(OTMS)$_2$]**$^{2+}$, and ^{3}**[Cu$_2$OH]**$^{3+}$; Tables S1–S9: X-ray crystallography data for ^{3}**[Cu$_2$Cl$_2$]**$^{2+}$, ^{2}**[Cu$_2$Cl$_2$]**$^{2+}$, ^{3}**[Cu$_2$(NCMe)$_2$]**$^{4+}$, ^{3}**[Cu$_2$Cl]**$^{3+}$, ^{3}**[Cu$_2$F]**$^{3+}$, ^{3}**[Cu$_2$(N$_3$)$_2$]**$^{2+}$, ^{3}**[Cu$_2$(ONO)$_2$]**$^{2+}$, ^{3}**[Cu$_2$(OTMS)$_2$]**$^{2+}$, and ^{3}**[Cu$_2$OH]**$^{3+}$, and Summary of structure determination of ^{3}**[Cu$_2$Cl$_2$]**$^{2+}$, ^{2}**[Cu$_2$Cl$_2$]**$^{2+}$,^{3}**[Cu$_2$(NCMe)$_2$]**$^{4+}$, ^{3}**[Cu$_2$Cl]**$^{3+}$, ^{3}**[Cu$_2$F]**$^{3+}$, ^{3}**[Cu$_2$(N$_3$)$_2$]**$^{2+}$, ^{3}**[Cu$_2$(ONO)$_2$]**$^{2+}$, ^{3}**[Cu$_2$(OTMS)$_2$]**$^{2+}$ **and** ^{3}**[Cu$_2$OH]**$^{3+}$.

Author Contributions: Conceptualization, N.C.T.; investigation, S.H.B., C.A.R., P.J.C. and M.R.G.; writing—original draft preparation, S.H.B.; writing—review and editing, N.C.T.; supervision, N.C.T.; funding acquisition, N.C.T. All authors have read and agreed to the published version of the manuscript.

Funding: This research was funded by the National Science Foundation, grant number 1945265.

Data Availability Statement: The data presented in this study are available in the Supplementary Materials.

Conflicts of Interest: The authors declare no conflict of interest. The funders had no role in the design of the study; in the collection, analyses, in the interpretation of data; in the writing of the manuscript; or in the decision to publish the results.

References

1. Tomkins, P.; Ranocchiari, M.; van Bokhoven, J.A. Direct Conversion of Methane to Methanol under Mild Conditions over Cu-Zeolites and beyond. *Acc. Chem. Res.* **2017**, *50*, 418–425.
2. Snyder, B.E.R.; Bols, M.L.; Schoonheydt, R.A.; Sels, B.F.; Solomon, E.I. Iron and Copper Active Sites in Zeolites and Their Correlation to Metalloenzymes. *Chem. Rev.* **2018**, *118*, 2718–2768.
3. Newton, M.A.; Knorpp, A.J.; Sushkevich, V.L.; Palagin, D.; van Bokhoven, J.A. Active sites and mechanisms in the direct conversion of methane to methanol using Cu in zeolitic hosts: A critical examination. *Chem. Soc. Rev.* **2020**, *49*, 1449–1486. [PubMed]
4. Solomon, E.I.; Heppner, D.E.; Johnston, E.M.; Ginsbach, J.W.; Cirera, J.; Qayyum, M.; Kieber-Emmons, M.T.; Kjaergaard, C.H.; Hadt, R.G.; Tian, L. Copper Active Sites in Biology. *Chem. Rev.* **2014**, *114*, 3659–3853.
5. Hoshikawa, R.; Mitsuhashi, R.; Asato, E.; Liu, J.; Sakiyama, H. Structures of Dimer-of-Dimers Type Defect Cubane Tetranuclear Copper(II) Complexes with Novel Dinucleating Ligands. *Molecules* **2022**, *27*, 576. [PubMed]
6. Mendy, J.S.; Saeed, M.A.; Fronczek, F.R.; Powell, D.R.; Hossain, M.A. Anion Recognition and Sensing by a New Macrocyclic Dinuclear Copper(II) Complex: A Selective Receptor for Iodide. *Inorg. Chem.* **2010**, *49*, 7223–7225.
7. Rhaman, M.M.; Alamgir, A.; Wong, B.M.; Powell, D.R.; Hossain, M.A. A highly efficient dinuclear Cu(II) chemosensor for colorimetric and fluorescent detection of cyanide in water. *RSC Adv.* **2014**, *4*, 54263–54267.
8. Mateus, P.; Lima, L.M.P.; Delgado, R. Di- and trinuclear copper(II) complexes of polyaza macrocycles and cryptands as anion receptors. *Polyhedron* **2013**, *52*, 25–42.
9. Haack, P.; Kärgel, A.; Greco, C.; Dokic, J.; Braun, B.; Pfaff, F.F.; Mebs, S.; Ray, K.; Limberg, C. Access to a Cu^{II}–O–Cu^{II} Motif: Spectroscopic Properties, Solution Structure, and Reactivity. *J. Am. Chem. Soc.* **2013**, *135*, 16148–16160.
10. Jurgeleit, R.; Grimm-Lebsanft, B.; Flöser, B.M.; Teubner, M.; Buchenau, S.; Senft, L.; Hoffmann, J.; Naumova, M.; Näther, C.; Ivanović-Burmazović, I.; et al. Catalytic Oxygenation of Hydrocarbons by Mono-μ-oxo Dicopper(II) Species Resulting from O−O Cleavage of Tetranuclear Cu^{I}/Cu^{II} Peroxo Complexes. *Angew. Chem. Int. Ed.* **2021**, *60*, 14154–14162.
11. Carsch, K.M.; Lukens, J.T.; DiMucci, I.M.; Iovan, D.A.; Zheng, S.-L.; Lancaster, K.M.; Betley, T.A. Electronic Structures and Reactivity Profiles of Aryl Nitrenoid-Bridged Dicopper Complexes. *J. Am. Chem. Soc.* **2020**, *142*, 2264–2276. [CrossRef]
12. Ziegler, M.S.; Lakshmi, K.V.; Tilley, T.D. Dicopper Cu(I)Cu(I) and Cu(I)Cu(II) Complexes in Copper-Catalyzed Azide–Alkyne Cycloaddition. *J. Am. Chem. Soc.* **2017**, *139*, 5378–5386. [CrossRef] [PubMed]
13. Ziegler, M.S.; Levine, D.S.; Lakshmi, K.V.; Tilley, T.D. Aryl Group Transfer from Tetraarylborato Anions to an Electrophilic Dicopper(I) Center and Mixed-Valence μ-Aryl Dicopper(I,II) Complexes. *J. Am. Chem. Soc.* **2016**, *138*, 6484–6491. [CrossRef]
14. Drew, M.G.B.; McCann, M.; Nelson, S.M. Bi-copper(I) and bi-copper(II) complexes of a 30-membered macrocyclic ligand: The inclusion of substrate molecules and the crystal and molecular structures of a μ-hydroxo- and a μ-imidazolato-complex. *J. Chem. Soc. Dalton Trans.* **1981**, 1868–1878. [CrossRef]
15. Drew, M.G.B.; McCann, M.; Nelson, S.M. Binuclear macrocyclic copper(II) complexes as receptors for small bridging ligands: X-ray crystal and molecular structure of a μ-azido complex. *J. Chem. Soc. Chem. Commun.* **1979**, 481–482. [CrossRef]
16. Drew, M.G.B.; Nelson, J.; Esho, F.; McKee, V.; Nelson, S.M. Dicopper(II) complexes of a macrocyclic ligand containing single hydroxo-, methoxo-, or 1,1-azido-bridges: Synthesis, magnetic properties, electron spin resonance spectra, and the crystal and molecular structure of a μ-hydroxo-derivative. *J. Chem. Soc. Dalton Trans.* **1982**, 1837–1843. [CrossRef]
17. Nelson, S.M.; Esho, F.S.; Drew, M.G.B. Metal-ion controlled reactions of 2,6-diacetylpyridine with 1,2-di-aminoethane and 2,6-diformylpyridine with o-phenylenediamine and the crystal and molecular structure of a pentagonal pyramidal cadmium(II) complex containing unidentate o-phenylenediamine. *J. Chem. Soc. Dalton Trans.* **1982**, 407–415. [CrossRef]
18. Cui, P.; Wang, Q.; McCollom, S.P.; Manor, B.C.; Carroll, P.J.; Tomson, N.C. Ring-Size-Modulated Reactivity of Putative Dicobalt-Bridging Nitrides: C−H Activation versus Phosphinimide Formation. *Angew. Chem. Int. Ed.* **2017**, *56*, 15979–15983. [CrossRef] [PubMed]
19. Liu, T.; Gau, M.R.; Tomson, N.C. Mimicking the Constrained Geometry of a Nitrogen-Fixation Intermediate. *J. Am. Chem. Soc.* **2020**, *142*, 8142–8146. [CrossRef] [PubMed]
20. Spentzos, A.Z.; Gau, M.R.; Carroll, P.J.; Tomson, N.C. Unusual cyanide and methyl binding modes at a dicobalt macrocycle following acetonitrile C–C bond activation. *Chem. Commun.* **2020**, *56*, 9675–9678. [CrossRef]

21. Thierer, L.M.; Brooks, S.H.; Weberg, A.B.; Cui, P.; Zhang, S.; Gau, M.R.; Manor, B.C.; Carroll, P.J.; Tomson, N.C. Macrocycle-Induced Modulation of Internuclear Interactions in Homobimetallic Complexes. *Inorg. Chem.* **2022**, *61*, 6263–6280. [CrossRef]
22. Wang, Q.; Zhang, S.; Cui, P.; Weberg, A.B.; Thierer, L.M.; Manor, B.C.; Gau, M.R.; Carroll, P.J.; Tomson, N.C. Interdependent Metal–Metal Bonding and Ligand Redox-Activity in a Series of Dinuclear Macrocyclic Complexes of Iron, Cobalt, and Nickel. *Inorg. Chem.* **2020**, *59*, 4200–4214. [CrossRef] [PubMed]
23. Zhang, S.; Cui, P.; Liu, T.; Wang, Q.; Longo, T.J.; Thierer, L.M.; Manor, B.C.; Gau, M.R.; Carroll, P.J.; Papaefthymiou, G.C.; et al. N−H Bond Formation at a Diiron Bridging Nitride. *Angew. Chem. Int. Ed.* **2020**, *59*, 15215–15219. [CrossRef]
24. Zhang, S.; Wang, Q.; Thierer, L.M.; Weberg, A.B.; Gau, M.R.; Carroll, P.J.; Tomson, N.C. Tuning Metal–Metal Interactions through Reversible Ligand Folding in a Series of Dinuclear Iron Complexes. *Inorg. Chem.* **2019**, *58*, 12234–12244. [CrossRef] [PubMed]
25. Wang, Q.; Brooks, S.H.; Liu, T.; Tomson, N.C. Tuning metal–metal interactions for cooperative small molecule activation. *Chem. Commun.* **2021**, *57*, 2839–2853. [CrossRef]
26. Römelt, C.; Weyhermüller, T.; Wieghardt, K. Structural characteristics of redox-active pyridine-1,6-diimine complexes: Electronic structures and ligand oxidation levels. *Coord. Chem. Rev.* **2019**, *380*, 287–317. [CrossRef]
27. Addison, A.W.; Rao, T.N.; Reedijk, J.; van Rijn, J.; Verschoor, G.C. Synthesis; structure, and spectroscopic properties of copper(II) compounds containing nitrogen–sulphur donor ligands; the crystal and molecular structure of aqua[1,7-*bis*(*N*-methylbenzimidazol-2′-yl)-2,6-dithiaheptane]copper(II) perchlorate. *J. Chem. Soc. Dalton Trans.* **1984**, 1349–1356. [CrossRef]
28. Alvarez, S. A cartography of the van der Waals territories. *Dalton Trans.* **2013**, *42*, 8617–8636. [CrossRef] [PubMed]
29. McKee, V.; Smith, J. Synthesis and X-ray structure of a bicopper(II) Schiff base macrocyclic complex having a single endogenous alkoxy bridge. *J. Chem. Soc. Chem. Commun.* **1983**, 1465–1467. [CrossRef]
30. Cheung, P.M.; Berger, R.F.; Zakharov, L.N.; Gilbertson, J.D. Square planar Cu(I) stabilized by a pyridinediimine ligand. *Chem. Commun.* **2016**, *52*, 4156–4159. [CrossRef]
31. Bower, J.K.; Cypcar, A.D.; Henriquez, B.; Stieber, S.C.E.; Zhang, S. C(sp^3)–H Fluorination with a Copper(II)/(III) Redox Couple. *J. Am. Chem. Soc.* **2020**, *142*, 8514–8521. [CrossRef] [PubMed]
32. Bower, J.K.; Cypcar, A.D.; Henriquez, B.; Stieber, S.C.E.; Zhang, S. Correction to "C(sp^3)–H Fluorination with a Copper(II)/(III) Redox Couple". *J. Am. Chem. Soc.* **2022**, *144*, 6118–6119. [CrossRef] [PubMed]
33. Chattopadhyay, S.; Ray, M.S.; Drew, M.G.B.; Figuerola, A.; Diaz, C.; Ghosh, A. Facile synthesis of Cu(II) complexes of monocondensed N,N,N donor Schiff base ligands: Crystal structure, spectroscopic and magnetic properties. *Polyhedron* **2006**, *25*, 2241–2253. [CrossRef]
34. Adhikary, C.; Mal, D.; Sen, R.; Bhattacharjee, A.; Gütlich, P.; Chaudhuri, S.; Koner, S. Synthesis, X-ray crystal structure and magnetic study of a novel μ_2-1,1-azido bridged dimeric copper(II) complex. *Polyhedron* **2007**, *26*, 1658–1662. [CrossRef]
35. Rahaman, S.H.; Bose, D.; Ghosh, R.; Mostafa, G.; Fun, H.-K.; Ghosh, B.K. Synthesis, crystal and molecular structures of 1D and 2D supramers of copper(II) with *N*,*N*′-{bis(pyridin-2-yl) benzylidene}butane-1,4-diamine. *Struct. Chem.* **2007**, *18*, 237–244. [CrossRef]
36. Nandy, M.; Shit, S.; Garribba, E.; Gómez-García, C.J.; Mitra, S. Double azido/cyanato bridged copper(II) dimers incorporating tridentate nitrogen donors Schiff base: Structure, EPR and magnetic studies. *Polyhedron* **2015**, *102*, 137–146. [CrossRef]
37. Camus, A.; Marsich, N.; Lanfredi, A.M.M.; Ugozzoli, F.; Massera, C. Copper(II)nitrito complexes with 2,2′-dipyridylamine. Crystal structures of the [(acetato)(2,2′-dipyridylamine)(nitrito-*O*,*O*′)copper(II)] and [(2,2′-dipyridylamine)(nitrito-*O*,*O*′)(μ-nitrito-*O*)copper(II)]$_2$·2(acetonitrile). *Inorg. Chim. Acta* **2000**, *309*, 1–9. [CrossRef]
38. Arnold, P.J.; Davies, S.C.; Durrant, M.C.; Griffiths, D.V.; Hughes, D.L.; Sharpe, P.C. Copper(II) nitrite complexes of tripodal ligands derived from 1,1,1-*tris*(2-pyridyl)methylamine. *Inorg. Chim. Acta* **2003**, *348*, 143–149. [CrossRef]
39. Zhu, R.-Q. Di-μ-nitrito-κ^4*O*:*O*-bis[bis(1-ethyl-1*H*-imidazole-κN^3)(nitrito-κO)copper(II)]. *Acta Crystallogr. E* **2011**, *67*, m869. [CrossRef]
40. Zhu, R.-Q. Bis(μ-nitrito-κ^2*O*:*O*)bis[bis(1-methyl-1*H*-imidazole-κN^3)(nitrito-κO)copper(II)]. *Acta Crystallogr. E* **2012**, *68*, m398. [CrossRef]
41. McGeary, M.J.; Wedlich, R.C.; Coan, P.S.; Folting, K.; Caulton, K.G. Synthesis and thermal decomposition of copper(I) silyloxide complexes. X-ray crystal structures of [Cu(OSiPh$_3$)]$_4$ and [Cu(OSiPh$_3$)(PMe$_2$Ph)]$_2$. *Polyhedron* **1992**, *11*, 2459–2473. [CrossRef]
42. Dai, X.; Warren, T.H. Dioxygen activation by a neutral β-diketiminato copper(I) ethylene complex. *Chem. Commun.* **2001**, *19*, 1998–1999. [CrossRef]
43. Kitajima, N.; Koda, T.; Iwata, Y.; Morooka, Y. Reaction aspects of a μ-peroxo binuclear copper(II) complex. *J. Am. Chem. Soc.* **1990**, *112*, 8833–8839. [CrossRef]
44. Kitajima, N.; Koda, T.; Hashimoto, S.; Kitagawa, T.; Morooka, Y. Synthesis and characterization of the dinuclear copper(II) complexes [Cu(HB(3,5-Me$_2$pz)$_3$)]$_2$X (X = O^{2-}, $(OH)_2^{2-}$, CO_3^{2-}, O_2^{2-}). *J. Am. Chem. Soc.* **1991**, *113*, 5664–5671. [CrossRef]
45. Chaudhuri, P.; Ventur, D.C.; Wieghardt, K.; Peters, E.M.; Peters, K. Preparation, Magnetism, and Crystal Structures of the Tautomers [LCu(μ_2-OH)$_2$CuL](ClO$_4$)$_2$ (Blue) and [LCu(μ_2-OH$_2$)(μ_2-O)CuL](ClOμ_4)μ_2 (Green): μ-Aqua-μ-oxo vs. Di-μ-hydroxo Linkage. *Angew. Chem. Int. Ed. Eng.* **1985**, *24*, 57–59. [CrossRef]

46. Thierer, L.M.; Wang, Q.; Brooks, S.H.; Cui, P.; Qi, J.; Gau, M.R.; Manor, B.C.; Carroll, P.J.; Tomson, N.C. Pyridyldiimine macrocyclic ligands: Influences of template ion, linker length and imine substitution on ligand synthesis, structure and redox properties. *Polyhedron* **2021**, *198*, 115044. [CrossRef] [PubMed]
47. Rosenau, C.P.; Jelier, B.J.; Gossert, A.D.; Togni, A. Exposing the Origins of Irreproducibility in Fluorine NMR Spectroscopy. *Angew. Chem. Int. Ed.* **2018**, *57*, 9528–9533. [CrossRef] [PubMed]